High-Latitude Precipitation: Snowfall Regimes at Two Distinct Sites in Scandinavia

JULIA A. SHATES,[a] CLAIRE PETTERSEN,[b] TRISTAN S. L'ECUYER,[a] STEVEN J. COOPER,[c] MARK S. KULIE,[d] AND NORMAN B. WOOD[b]

[a] *Department of Atmospheric and Oceanic Sciences, University of Wisconsin–Madison, Madison, Wisconsin*
[b] *Space Science and Engineering Center, University of Wisconsin–Madison, Madison, Wisconsin*
[c] *University of Utah, Salt Lake City, Utah*
[d] *Advanced Satellite Products Branch, NOAA/NESDIS/Center for Satellite Applications and Research, Madison, Wisconsin*

(Manuscript received 23 October 2020, in final form 1 June 2021)

ABSTRACT: The prevailing snowfall regimes at two Scandinavian sites, Haukeliseter, Norway, and Kiruna, Sweden, are documented using ground-based in situ and remote sensing methods. Micro Rain Radar (MRR) profiles indicate three distinct snowfall regimes occur at both sites: shallow, deep, and intermittent snowfall. The shallow snowfall regime produces the lowest mean snowfall rates and radar echo tops are confined below 1.5 km above ground level (AGL). Shallow snowfall occurs under areas of large-scale subsidence with a moist boundary layer and dry air aloft. The atmospheric ridge coinciding with shallow snowfall is highly anomalous over Haukeliseter but is more common in Kiruna where shallow snowfall was frequently observed. The shallow snowfall particle size distributions (PSDs) are broad with lower particle concentrations than other regimes, especially small particles. Deep snowfall events exhibit MRR profiles that extend above 2 km AGL and tend to be associated with weak low pressure and high relative humidity throughout the troposphere. The PSDs in deep events are narrower with high concentrations of small particles. Increasing MRR reflectivity toward the surface suggests aggregation as a possible growth process during deep snowfall events. The heaviest mean snowfall rates are associated with intermittent events that are characterized by deep MRR profiles but have variations in intensity and height. The intermittent regime is associated with anomalous, deep low pressure along the coast of Norway and enhanced relative humidity at lower levels. The PSDs reveal high concentrations of small and large particles. The analysis reveals that there are unique characteristics of shallow, deep, and intermittent snowfall regimes that are common between the sites.

KEYWORDS: Atmosphere; Europe; Precipitation; Snow; Snowfall; Winter/cool season; Cloud microphysics; Drop size distribution; Freezing precipitation; In situ atmospheric observations; Microwave observations; Radars/Radar observations; Remote sensing; Surface observations; Field experiments

1. Introduction

Snowfall plays an important role in climate and society. Snow cover influences global energy balance and atmospheric circulation (Vavrus 2007), and, through boundary layer interactions, it influences synoptic-scale disturbances (Rydzik and Desai 2014) and springtime turbulent fluxes (Lund et al. 2017). Snowfall is the source of mountain snowpack (Knowles et al. 2006) and is critical for water and power resources that depend on wintertime accumulation. In Scandinavia, 75%–100% of the precipitation falls as snow during winter months (Field and Heymsfield 2015), and Norway and Sweden depend on 94% and 65% of energy resources from hydropower (Instanes et al. 2016). Additionally, snow holds cultural and socioeconomic value to the northern Sámi people (Riseth et al. 2011; Eira et al. 2013).

The future of winter precipitation in the high latitudes is uncertain as the Arctic warms more quickly than the rest of the globe (Collins et al. 2013; Serreze and Barry 2011). Changes in snowfall will impact surface albedo (Screen and Simmonds 2012), terrestrial snow cover and depth (Park et al. 2013), and freshwater inputs to the Arctic Ocean through runoff (Rawlins et al. 2006, 2010). While precipitation is generally expected to increase in the high latitudes (Liu et al. 2012; Bintanja and Selten 2014), there are challenges and biases in projecting snowfall in global climate models (Kay et al. 2018), and while some regions may experience increases in snow accumulation, others may shift from snow to rain (Bintanja and Andry 2017; Tamang et al. 2020). In Scandinavia, changes in winter precipitation, such as a shift from snow to midwinter rain, would impact water and power resources (Instanes et al. 2016), and high-latitude ecosystems (Putkonen and Roe 2003; Sokolov et al. 2016). In addition to the phase of precipitation, the weather systems that bring precipitation to high-latitude regions are also projected to change. Moisture intrusions from lower latitudes (i.e., atmospheric rivers) interact with topography and result in extreme precipitation (Sodemann and Stohl 2013; Guan and Waliser 2015) and are projected to increase in frequency in the North Atlantic Ocean region (Lavers et al. 2013).

Observations of snowfall are needed to better understand the current state of the climate, and to constrain climate models for future projections. However, snowfall remains challenging to observe and measure accurately. Wind impacts the accuracy of accumulation measurements (Liston and Sturm 2004; Rasmussen et al. 2012; Wolff et al. 2015) and redistributes snow

Corresponding author: Julia A. Shates, shates@wisc.edu

DOI: 10.1175/JAMC-D-20-0248.1

on the surface (Elder et al. 1991), especially in mountainous regions. At high latitudes, these issues are exacerbated by the scarcity of ground-based observations (Schneider et al. 2014). Networks of scanning weather radars observe precipitation but are affected by beam blockage around mountainous regions (Smalley et al. 2014), and radar beams often overshoot shallow snowfall because of the range effects (Norin et al. 2015, 2017; Pettersen et al. 2020a). Satellites such as *CloudSat* (Stephens et al. 2002) and the Global Precipitation Measurement (GPM) *Core Observatory* (Hou et al. 2014) provide near-global coverage, but are limited in latitudinal range, infrequently pass over the same groundtrack, and the satellite blind zone prevents space-based radars from detecting snowfall below 1–1.5 km above the surface because of ground clutter (Kulie and Bennartz 2009). The GPM Dual-Frequency Precipitation Radar was found to underestimate solid precipitation due to radar sensitivity, especially over complex terrain (Speirs et al. 2017). In addition, it is difficult to distinguish between falling snow and emissions from snow-covered surfaces using passive microwave sensors (Skofronick-Jackson et al. 2013). In polar regions, studies have documented that snowfall rates and number of events are underestimated because of the blind zone (Maahn et al. 2014; Bennartz et al. 2019; McIlhattan et al. 2020). Ground-based observations are needed to assess satellite snowfall retrievals (Maahn et al. 2014; von Lerber et al. 2018; Lemonnier et al. 2019), to validate and support new snowfall retrieval algorithm versions (Skofronick-Jackson et al. 2015; Houze et al. 2017), and to constrain and evaluate snowfall in global climate models (Kay et al. 2018).

Field campaigns have been used at various sites in the midlatitudes, high latitudes, and in complex terrain, including lake-effect snow (LeS) (Kristovich et al. 2017; Skofronick-Jackson et al. 2015) and storms interacting with mountains (Houze et al. 2017). Ground-based observations have effectively identified unique snowfall regimes in different locations such as the Greenland ice sheet (Pettersen et al. 2018), the U.S. Great Lakes region (Pettersen et al. 2020a), Antarctica (Durán-Alarcón et al. 2019; Gorodetskaya et al. 2014), and complex terrain in Scandinavia (Schirle et al. 2019). In addition, spaced-based and weather radar network observations support the existence and utility in identifying snowfall regimes (Kulie et al. 2016; Norin et al. 2017; McIlhattan et al. 2020). A deeper understanding of regime-dependent microphysical characteristics is important to improve snowfall forecasting, as accumulation depends on snowfall density properties such as habit, degree of riming, particle size distribution, and number concentration (Roebber et al. 2003). Radar estimates of snowfall rates are improved when microphysical characteristics are incorporated in retrievals (Cooper et al. 2017; Souverijns et al. 2017; Schirle et al. 2019).

Even with these sites and studies, snowfall data gaps remain in the vast, undersampled high latitudes. This work provides new insights into snowfall processes using observations at two distinct ground-based sites in Scandinavia: Haukeliseter, Norway, and Kiruna, Sweden. The Scandinavian Peninsula is located near the end of the North Atlantic storm track, which suggests the likelihood of multiple extratropical storms bringing precipitation to the region (Hoskins and Hodges 2002). Schirle et al. (2019) showed how wind direction in a snowfall event in Haukeliseter influences snowfall characteristics and retrievals of accumulation. In this study, we aim to address the following questions to better understand snowfall processes: How are snowfall regimes similar and different in varying regions in the high latitudes? How is the macro- and microphysical character of snowfall influenced by the local environment versus the larger synoptic-scale weather patterns? This research provides complementary new insights to the current body of work on snowfall by leveraging observations to form connections between the microphysical characteristics of snowfall with the meteorological measurements, synoptic-scale conditions, and thermodynamic profiles. Section 2 describes the sites, instrumentation, data, and methods. Section 3 explores characteristics of snowfall regimes separated by site. Section 4 discusses similarities and differences between snowfall regimes at the sites. Section 5 discusses the key results and their implications for snowfall research, and possible future uses for these ground-based remote sensing and in situ observations.

2. Site description and instrument suite

An instrument suite was deployed at the Haukeliseter Test site managed by the Norwegian Meteorological Institute (Met Norway) from September 2016 to June 2017. The Haukeliseter site is on a mountain plateau at 991 m elevation in the Telemark region of Norway (59.81°N, 7.21°E), which is located in complex, mountainous terrain with deep coastal fjords to the west (Fig. 1). During an average winter in Haukeliseter, snow depth can be between 1.5 and 2 m. Also, the site commonly experiences high winds; a nearby station reported a significant number of snow events with maximum winds exceeding 15 m s^{-1} over a 10-yr period (Wolff et al. 2015). Met Norway manages multiple instruments at this site for measuring precipitation, temperature, and wind. Additional instruments were deployed at the site, including the Micro Rain Radar (MRR) and the Precipitation Imaging Package (PIP) as part of the High-Latitude Measurement of Snowfall (HiLaMS) field campaign (Schirle et al. 2019). The MRR and PIP, were located 6 m above the ground (Fig. 1).

The second site for this study is located in Kiruna, Sweden. Kiruna is above the Arctic circle (67.84°N, 20.41°E) and the site is at 530-m elevation (Fig. 1). The surrounding region is forested with proglacial lakes. Sweden's highest mountains are approximately 75 km southwest of Kiruna. The snowfall instruments were deployed October 2017 to May 2018 at the Swedish Institute for Space Physics (IRF), which manages a permanent weather station. The MRR was located on top of a four-story building, and the PIP was approximately 0.4 km away atop a one-story building (4 m above the ground).

a. MRR

The METEK MRR 2 is a vertically profiling 24-GHz (K band) frequency-modulated, continuous wave Doppler radar (Klugmann et al. 1996). The MRR has low power consumption

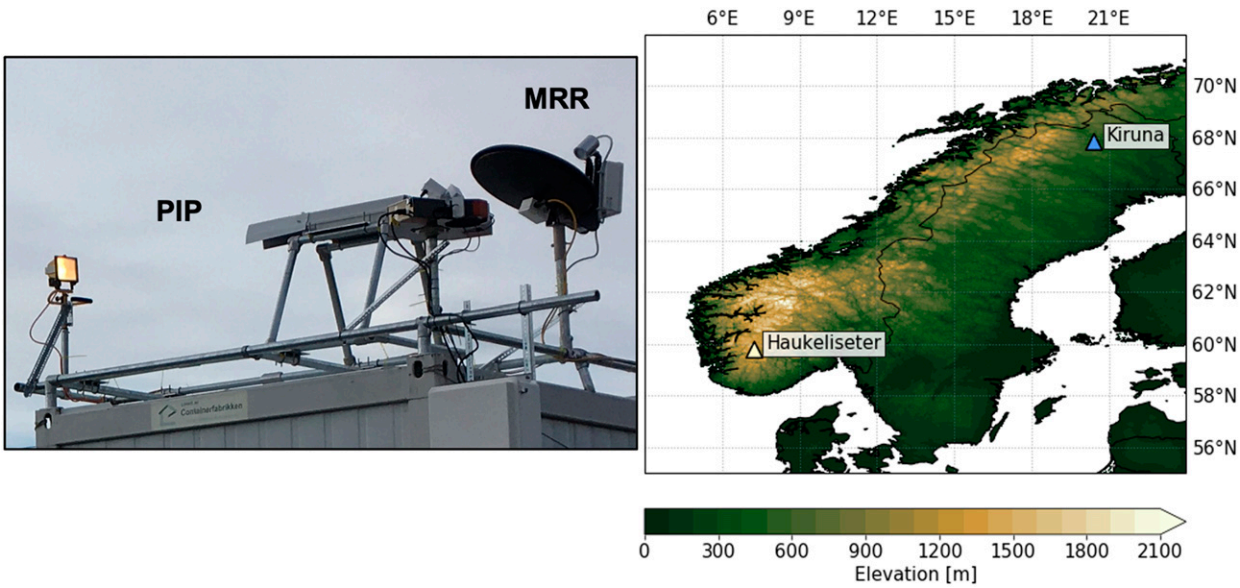

FIG. 1. (left) Photograph of the MRR on the right and PIP on the left taken at the Haukeliseter site. (right) A topographic map of the Scandinavian Peninsula in meters MSL. The triangles with labels mark the respective site locations.

of 25 W (200 W with a heated dish to prevent snow accumulation), is portable, and requires minimal maintenance, which is advantageous for snowfall studies in remote regions (Kneifel et al. 2011; Maahn and Kollias 2012). The Maahn and Kollias (2012) method was used to improve sensitivity of the MRR observations from 3 dBZ (Kneifel et al. 2011) to −10 dBZ because global observations of snowfall are often less than 3 dBZ (Kulie and Bennartz 2009). The processing method provides 1-min resolution equivalent radar reflectivity factor (hereinafter, radar reflectivity Z_e; dBZ), Doppler velocity V_d (m s^{-1}) and spectral width (m s^{-1}). The MRR profiles up to 3 km above ground level (AGL) with 100-m range resolution, but data below 300 m AGL are removed due to ground clutter. The snowfall rate S in liquid water equivalent (LWE) (mm h^{-1}) is calculated from the reflectivity profile at 400 m AGL using a Z_e–S relationship for dry snowfall (Matrosov 2007):

$$Z_e = 56S^{1.2}. \tag{1}$$

The minimum detectable snow rate is 0.01 mm h^{-1} after the Maahn and Kollias method of processing the spectra. The Z_e–S relationship in Eq. (1) was originally developed for a 35.5-GHz (Ka band) vertically profiling cloud radar, but Kneifel et al. (2011) showed that Eq. (1) can be effectively used with the MRR reflectivity and has a 7% overestimation. In addition, the Z_e–S relationship was established for dry snowfall but can be applied to events with a small amount of riming (Matrosov 2007). It is important to note that the use of this Z_e–S relationship contains uncertainties and is not necessarily suitable for all snowfall regimes. However, it provides a measure with which we can make comparisons between snowfall regimes and measurements.

In addition to the LWE from the Z_e–S relationship, the MRR observations are used in a snowfall retrieval technique used by Schirle et al. (2019, hereinafter S19). The S19 method uses an optimal estimation approach (Rodgers 2000) that combines radar reflectivities, in situ observations, atmospheric temperature profiles, and a priori information into a common retrieval framework to provide an estimate of snowfall properties consistent with each. The retrieval was optimized using data from distinct snowfall events in Haukeliseter, which may result in uncertainties in retrieving snowfall for other events and locations (i.e., Kiruna). The S19 method was originally developed by Cooper et al. (2017) with a Ka-band radar but was modified for the MRR in S19. Two particle models for aggregates developed for the *CloudSat* mission are used for this work, six-branched porous, flattened rosette-like (b6pf) and eight-branched porous rosette-like (b8pr-30) (hereinafter respectively S19b6 and S19b8). The S19b6 particle model produces higher reflectivities per unit mass relative to the S19b8 (Schirle et al. 2019) and is more consistent with rimed snow particles. The S19b8 model is more representative of drier snow conditions. Wood et al. (2015) provide a thorough description of these particle models.

b. PIP

The PIP (Newman et al. 2009; Pettersen et al. 2020b) is a custom NASA video imager with a high-speed camera (380 frames per second) encased in a housing facing a bright halogen lamp 2 m away (pictured in Fig. 1). The image resolution is approximately 0.1 mm × 0.1 mm, and the focal plane is located 1.33 m away from the camera lens. As snowflakes fall freely through this open volume, the camera essentially captures videos of shadows of the hydrometeors that are shades of gray. Processing the videos provides precipitation products: particle size distributions (PSDs) and particle velocity distributions (VVDs) at 1 min resolution (von Lerber et al. 2017, 2018;

Pettersen et al. 2020b). The PSDs are derived from counts of particles falling through the volume that are organized by particle sizes ranging from 0.2 to 26 mm in 0.2-mm size bins. The particle size is represented as area-equivalent diameter D, which is the diameter of a circle with the same area as the observed particle. The VVDs are a measure of the mean particle velocities within each size bin ($\mathrm{m\,s^{-1}}$) for each minute. The mean fall speed as a function of D is obtained from the VVDs. Relative to methods using inlets or gauges to measure precipitation, the effects of wind are reduced without the need for a fence because the setup permits snowflakes to fall into the open volume unimpeded (Newman et al. 2009; Pettersen et al. 2020a). In addition, the PIP can determine precipitation phase, phase-separated snow and rain rates in LWE, and snow density (Tiira et al. 2016; von Lerber et al. 2018; Pettersen et al. 2020b).

c. Surface meteorological observations

Meteorological observations (wind speed and direction, accumulation, air temperature) for the Haukeliseter site were provided by Met Norway. The setup of the surface meteorological instruments can be found in Wolff et al. (2015). Multiple anemometers are deployed on 4.5- and 10-m masts; in this work we use wind measurements taken on mast 1 at 10 m from a Gill WindObserver II. The accuracy of wind speed and direction for this sensor is ±2% at $12\,\mathrm{m\,s^{-1}}$. Snow accumulation is measured as LWE from an automated Geonor precipitation gauge (Geonor T-200BM) shielded by a double fence, which fulfills official requirements for the Double Fence Automated Reference (DFAR) (Wolff et al. 2015). The sensitivity of this precipitation gauge is 0.075 mm with 0.1% accuracy. Snowfall measurements are sensitive to wind especially around instrumentation, but the wind fences reduce this impact (Rasmussen et al. 2012). The temperature is measured at gauge height by a pt100 element protected by a standard Norwegian radiation screen (Wolff et al. 2015).

Meteorological data for Kiruna are available online from the IRF (http://www2.irf.se/weather/). The instrumentation consists of a Vaisala, Inc., WXT536, which provides 1-min observations of wind speed and direction, surface temperature, and relative humidity at 2 m AGL. There were some quality control issues with the wind measurements at temperatures below −15°C, which are under investigation (U. Raffalski 2020, personal communication). The measurement accuracies for sensors are ±3% for wind speed and direction at $10\,\mathrm{m\,s^{-1}}$ and ±0.3°C for temperature at 20°C.

d. Reanalysis data

This study uses the ECMWF ERA5 reanalysis products (Copernicus Climate Change Service 2017) to characterize the synoptic conditions for the snowfall regimes. The variables used in this work include hourly products for 2 m (surface) temperature, mean sea level pressure (MSLP), 500-hPa geopotential height Z_{500}, and vertical profiles of temperature and relative humidity (RH). For the thermodynamic profiles and surface temperature, the closest ERA5 coordinates to the sites used in this study are 60°N, 7.25°E for Haukeliseter, and 68°N, 20.5°E for Kiruna. The spatial resolution of ERA5 is 31 km globally, and there are 37 vertical levels. Hourly anomalies are calculated from monthly means from 1979 to 2018 (climatological period). To adjust for elevation in the ERA5 vertical profiles, the surface pressure values were determined from the winter mean sea level pressure during the climatological period. The Haukeliseter and Kiruna surfaces are at 875 and 950 hPa, respectively.

3. Methods

A radar reflectivity threshold of −10 dBZ is used to determine precipitation occurrence. In this work, we identify samples of snowfall events that fit into three regimes: shallow, deep, and intermittent. Start and end time of events were determined by the MRR radar reflectivity profiles, and events were required to have a minimum duration of 1 h. Rain and snow events were separated by a surface temperature threshold of 2°C (Liu 2008; Pettersen et al. 2020a) and by excluding events with clear evidence of rain in the MRR reflectivity and Doppler velocity profiles. Precipitation echo-top height AGL is the first threshold to distinguish snowfall regimes. Shallow snowfall events have echo-top heights defined below 2 km AGL. The deep events are those that exceed 2 km AGL and echoes commonly reach the maximum height of the MRR operating range height (3 km AGL). The intermittent snowfall events also exceed 2 km AGL, but temporal variations distinguish the deep and intermittent snowfall regimes. Specifically, the deep snowfall events have moderate and continuous snowfall during an event, while the intermittent snowfall alternates between intervals of higher and lower values of reflectivity throughout time. Schirle et al. (2019) previously described that the pulses of heavier snowfall typically occurred 30–45 min in Haukeliseter with reflectivity values greater than 25 dBZ for a heavy pulse and less than 15 dBZ for a light pulse. In Kiruna, the pulsed timing is more variable, occurring between 15 min and 1 h, and the reflectivity values are lower than in Haukeliseter, ranging from greater than 20 dBZ for a heavy pulse and less than 10 dBZ for light. Several studies have described vertical cloud or precipitation structure as a way to separate snowfall regimes. Kulie et al. (2016) showed differences in shallow cumuliform and deep nimbostratus using cloud-layer height AGL. Most of the shallow cumuliform occurs below 2 km AGL, whereas the frequency of the cloud-layer height for deep snowfall is highest for 4 km AGL. The height distribution of nimbostratus snowfall is broad and has some overlap with shallow cumuliform. Pettersen et al. (2020a) showed that shallow (LeS) snowfall generally occurred below 1.5 km AGL. Jeoung et al. (2020) showed three snowfall producing cloud regimes at a site in South Korea: near surface (cloud tops < 1.5 km AGL), shallow (cloud tops between 1.5 and 4 km AGL), and deep (cloud tops > 4 km AGL).

Figures 2a–c exemplify MRR time series for the three regimes. Figures 2d–f show that regime separations are also apparent in the PIP PSDs. The deep snowfall regime has the most small particles when compared with the shallow and intermittent regimes, the PIP captures larger and fewer particles for

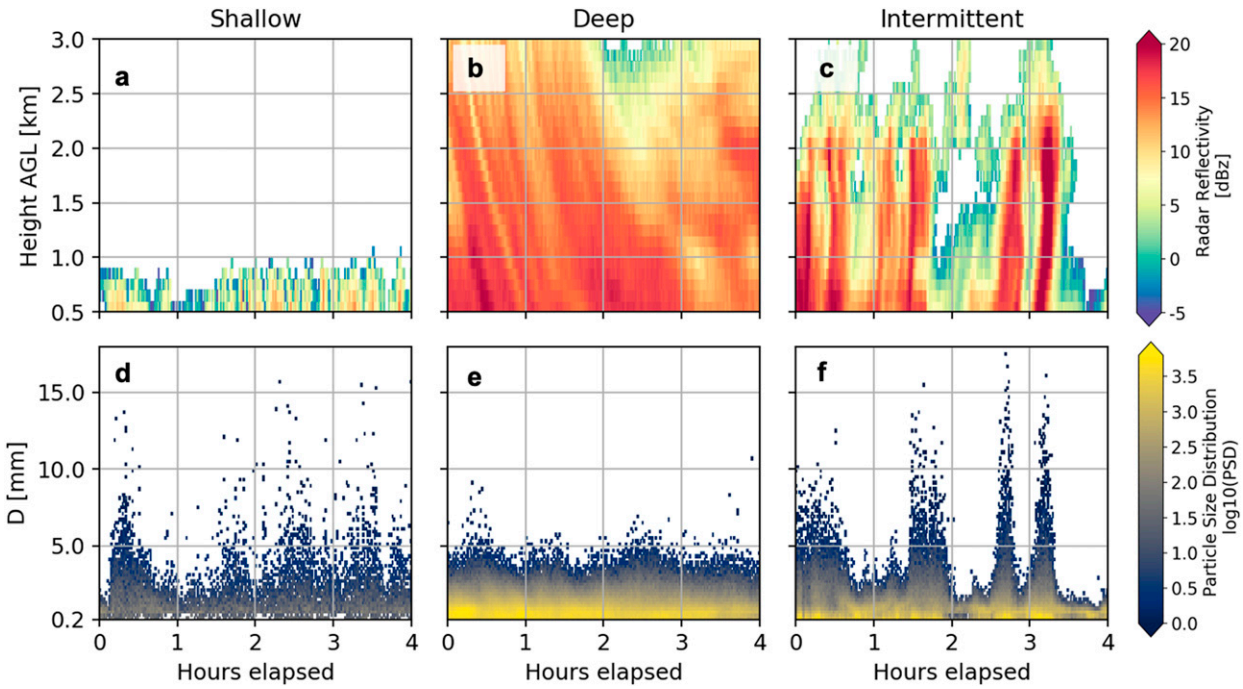

FIG. 2. Examples of the 4 h of observations for (left) shallow, (center) deep, and (right) intermittent snowfall regimes in three separate samples of (a)–(c) MRR and (d)–(f) PIP observations. The y axis for the MRR profile time series of radar reflectivity is height AGL. The y axis for the PIP PSD time series is D. The 4-h samples of coincident MRR and PIP observations are from Kiruna.

shallow snowfall, and the intermittent contains both small and large particles and also varies temporally.

4. Results

a. Haukeliseter

Table 1 shows the duration and number of events for the regimes and the mean snowfall rates from retrievals and observations. The shallow snowfall regime includes 10 distinct events, the events are relatively long-lasting, and the total number of hours (135) exceeds the deep snowfall, for which there are 19 events with mean duration of 5.4 h. However, the deep events produce moderate accumulation (mean values between 0.67 and 1.1 mm h^{-1} for retrievals and measurements), while the shallow snowfall is associated with lighter snowfall (mean values between 0.08 and 0.17 mm h^{-1}), so the contribution to accumulation is lower (see the appendix for event accumulations). The intermittent snowfall regime includes 13 distinct events (299 h total), and highest snowfall rates (mean values between 1.04 and 2.41 mm h^{-1}) thus contributing to large accumulations. The PIP observes lower mean snowfall rates for the shallow and deep regimes. However, mean LWE for rates vary for events and there are also missing events due to instrument downtime (see appendix for event details and instrument downtime).

1) SNOWFALL CHARACTERISTICS

The MRR profiles of reflectivity, Doppler velocity, and spectral width illustrate differences between the snowfall regimes (Fig. 3). The results from the MRR in this study are presented as 2D histograms. The 2D histogram for the shallow snowfall regime shows that the precipitation echo tops extend to approximately 1.5 km AGL where the reflectivity ranges from 0 to 5 dBZ (Fig. 3a). At 0.5 km AGL, the range broadens to span from −5 to 15 dBZ. The majority of the MRR Doppler velocities for the shallow regime are between 0.5 and 1.5 m s^{-1}, with some as low as −1 m s^{-1} implying some upward motions and particles moving away from the radar (Fig. 3b). At 0.5 km AGL, the spectral width is relatively broad ranging from 0.2 to 0.7 m s^{-1} (Fig. 3c).

The reflectivity profile for the deep snowfall regime (Fig. 3d) shows increasing radar reflectivity with decreasing height. At 3 km AGL, the reflectivity ranges from 0 to 10 dBZ, which broadens and increases with decreasing height with most observations between 10 and 20 dBZ at 0.5 km AGL. The majority of Doppler velocities are relatively invariant and near 1 m s^{-1} throughout the column, but the histogram reveals values as high as 1.5 m s^{-1} and updrafts of −0.5 m s^{-1} throughout the column (Fig. 3e). The spectral width profile is relatively narrow throughout the column, with values from 0.2 to 0.4 m s^{-1} and maximum values of 0.6 m s^{-1} below 1 km AGL (Fig. 3f).

The intermittent snowfall regime contains a broad range of radar reflectivity throughout the column from −5 to 25 dBZ, but it is dominated by high reflectivities (>10 dBZ) below 1.5 km AGL (Fig. 3g). The alternating high and low reflectivities (see Fig. 2c) result in the broad range seen in the

TABLE 1. Summary of snowfall regimes for Haukeliseter (Hauk) and Kiruna (Kir). The Z_e–S, S19b6, S19b8, PIP, and DFAR columns show the mean of the snowfall rates for each regime. Note that the PIP and DFAR experienced downtime during the winter in Haukeliseter; the mean snowfall rates for the regimes do not include all of the events. Individual event duration, accumulations, and instrument downtime are listed in the appendix. The X symbol indicates missing observations or retrievals for the event.

Regime and location	Total events	Total hours	Avg duration	Max/min duration	Z_e–S (mm h^{-1})	S19b6 (mm h^{-1})	S19b8 (mm h^{-1})	PIP (mm h^{-1})	DFAR (mm h^{-1})
Shallow Hauk	10	135	13.5	34/2	0.14	0.1	0.13	0.08[a]	0.17
Deep Hauk	19	103	5.4	24/1	0.77	0.66	1.1	0.33	0.67
Intermittent Hauk	13	299	23	47/14	1.14	1.04	1.7	2.41	0.73
Shallow Kir	25	486	19.4	83/2	0.12	0.1	0.15	0.07	X
Deep Kir	23	180	7.8	31/2	0.38	0.33	0.52	0.4	X
Intermittent Kir	3	101	34	61/10	0.47	0.39	0.64	0.43	X

[a] The PIP mean snowfall rate for shallow snowfall in Haukeliseter represents only two events.

composite 2D histogram unlike the deep snowfall regime. The Doppler velocities are indicative of substantial turbulence (Fig. 3h) ranging from $-1\,\mathrm{m\,s^{-1}}$ (away from the radar) to $1.5\,\mathrm{m\,s^{-1}}$ (toward the radar), with the majority of the observations between 0 and $1\,\mathrm{m\,s^{-1}}$. Figure 3i shows that the spectral width for the intermittent snowfall regime is broad, especially at lower levels, with a maximum reaching $1.2\,\mathrm{m\,s^{-1}}$ at 0.5 km AGL, much higher than for the other regimes.

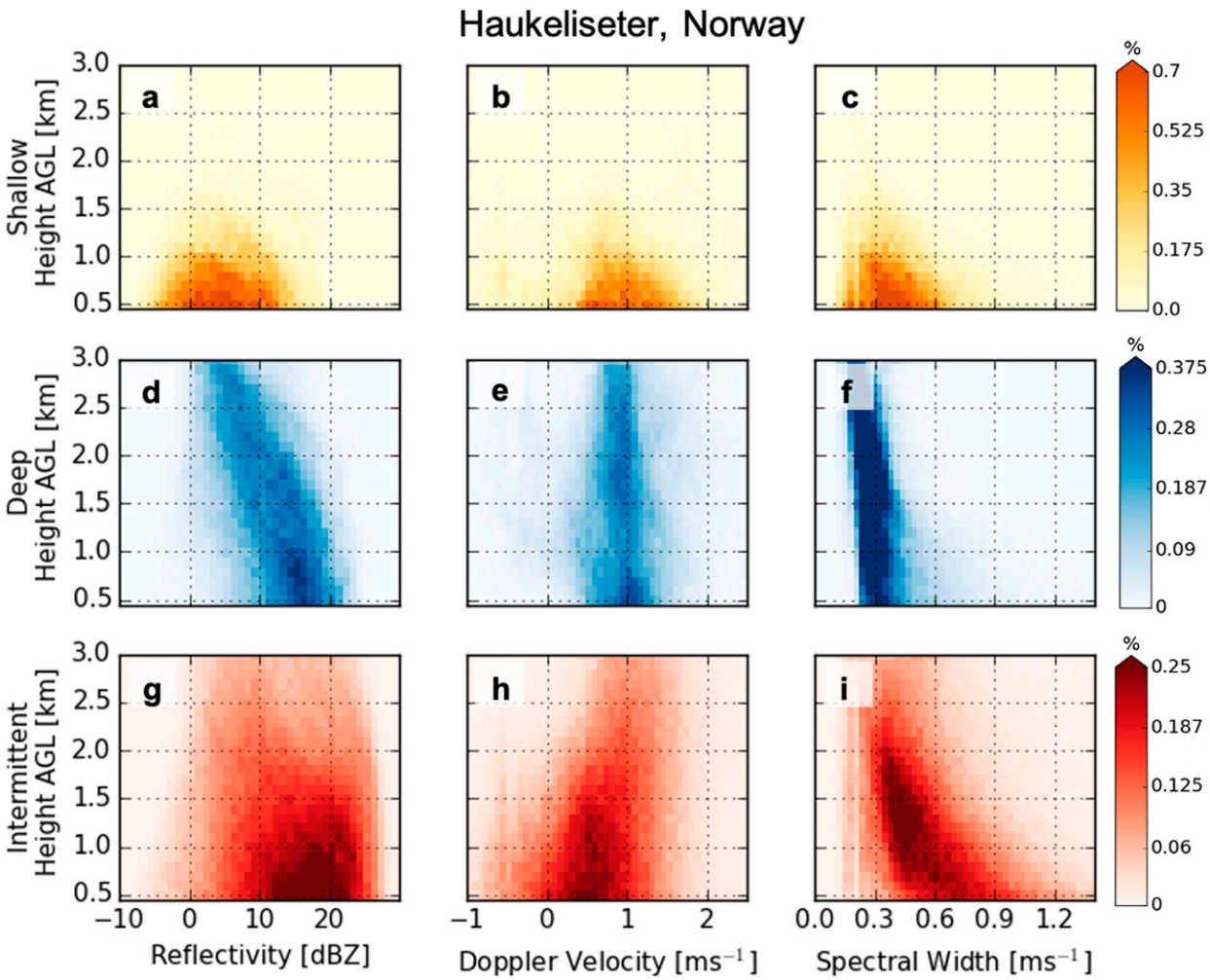

FIG. 3. Radar profiles of snowfall regimes in Haukeliseter expressed as 2D histograms for the (a)–(c) shallow, (d)–(f) deep, and (g)–(i) intermittent regimes. The 2D histograms from MRR profiles include (left) radar reflectivity, (center) Doppler velocity, and (right) spectral width. The 2D histograms compress the profiles across the time series to illustrate the relationship with height. Each histogram is normalized by total observations in each snowfall regime.

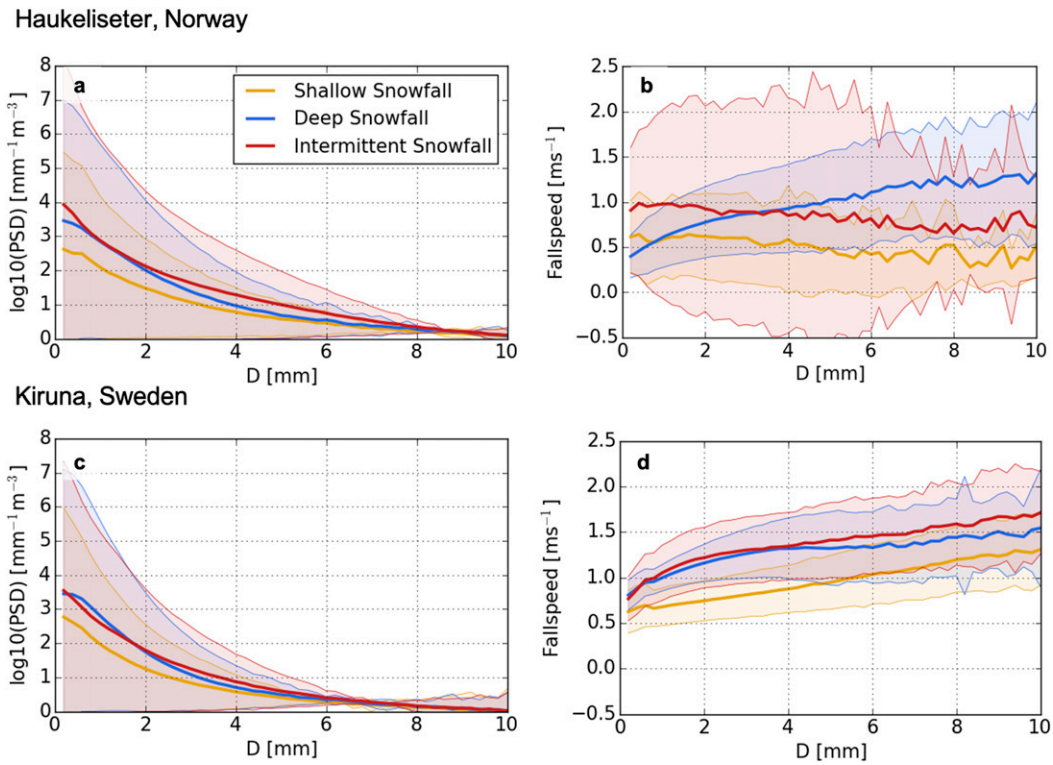

FIG. 4. The (a),(b) Haukeliseter and (c),(d) Kiruna PIP snowfall regime characteristics, showing (left) the mean PSD as a function of D for all PIP observations separated out in each regime and (right) the mean fall speeds for each snowfall regime. The shallow, deep, and intermittent regimes are yellow, blue, and red, respectively. The shaded regions illustrate 1 standard deviation from the mean. There are missing PIP observations in Haukeliseter because of instrument downtime. Table A1 in the appendix indicates instrument uptime for the events. The variation in mean fall speeds for particles > 6 mm may be because of the fact that there are fewer larger particles being observed.

The PIP-derived mean PSDs and fall speeds reveal differences in the microphysical characteristics for the shallow, deep, and intermittent snowfall regimes (Figs. 4a,b). In general, the mean PSD for the shallow regime has a lower particle concentration across all values of D relative to the deep and intermittent regimes. The deep regime mean PSD is relatively narrow with a maximum concentration of smaller particles ($D < 0.4$ mm) of $10^{3.5}\,\mathrm{m^{-3}\,mm^{-1}}$. For particles with $D < 0.4$ mm, the intermittent snowfall regime particle concentration is $10^4\,\mathrm{m^{-3}\,mm^{-1}}$. The shallow snowfall regime has fewer smaller particles by one order of magnitude than the two other regimes. The intermittent snowfall regime has the largest particle concentrations across all particle sizes. For shallow snow, the mean fall speeds are relatively constant and low ($<0.5\,\mathrm{m\,s^{-1}}$) and vary the least in comparison with the other two regimes. The mean fall speed for the deep snowfall regime increases from 0.5 to $1.25\,\mathrm{m\,s^{-1}}$ for particles from $D < 1$ to 10 mm. The mean fall speed values for the intermittent snowfall regime are $1\,\mathrm{m\,s^{-1}}$ for particles smaller than 2 mm but gradually decrease to $0.75\,\mathrm{m\,s^{-1}}$ with increasing particle size. However, the intermittent snowfall regime has the largest variation in fall speeds, ranging from -0.5 to $2\,\mathrm{m\,s^{-1}}$.

2) METEOROLOGICAL OBSERVATIONS AND ATMOSPHERIC CIRCULATION

To understand the differences in the snowfall characteristics of each regime, we examine the general environmental conditions present. The box-and-whisker plots of ERA5 2-m temperature for winter months from 1979 to 2018, shown in Fig. 5a, provide climatological context of the temperatures at the two sites. The mean ERA5 2 m temperatures for the deployment periods are shown as black stars to compare with the climatology. In Haukeliseter (yellow boxes), the mean deployment month temperatures are within the interquartile range except for December 2016, which is above the 75th percentile of climatological temperature.

The range of observed surface temperatures in Haukeliseter vary for the shallow, deep, and intermittent snowfall regimes (Fig. 5b, yellow boxes). The ERA5 2 m mean temperature values for the snowfall regimes are also shown as black triangles superimposed on the box-and-whisker plot for comparison. The shallow snowfall regime is the coldest with a mean of −5.7°C, and a comparatively broad range of values, from 1.5° to −15°C. The deep snowfall regime has a narrower and warmer range of temperatures relative to the shallow snow,

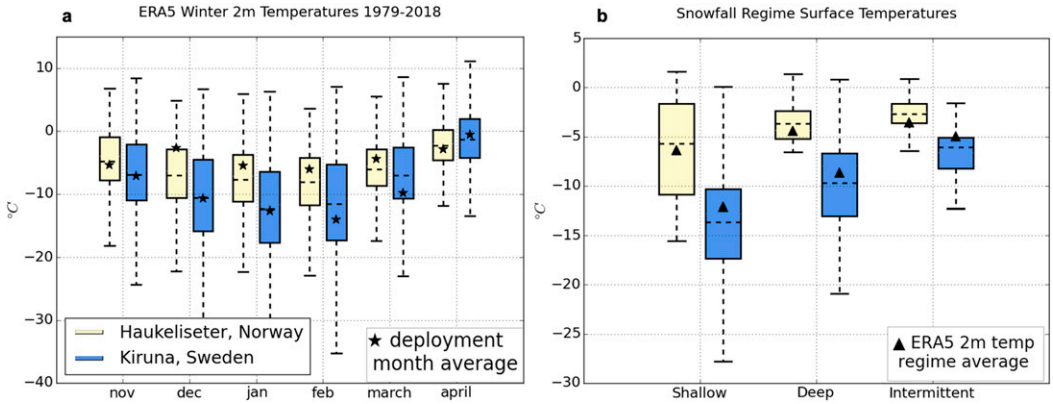

FIG. 5. (a) The monthly ERA5 2-m temperature distributions for winter months (November–April) for 1979–2018 at Haukeliseter (59.81°N, 7.21°E) and Kiruna (67.84°N, 20.41°E). The horizontal dashed lines in the boxes represent the climatological mean temperature of the months. The boxes span the 25th and 75th percentile range, and the whiskers show the range of the 95th and 5th percentile. The black stars are the mean ERA5 mean temperature during the month and year of the deployments at each site. (b) The mean surface temperature distributions from ground-based observations at each site during distinct snowfall regimes (shallow, deep, and intermittent). The boxes have the same interquartile range as in (a) (25th and 75th percentile); the horizontal dashed lines in the boxes are mean temperature for all compiled samples for each regime. The black triangles are the ERA5 2-m mean temperature for those regimes.

with a mean observed surface temperature of −3.7°C. Intermittent snowfall has a similar temperature range to deep snowfall, but the distribution is narrower and slightly warmer. The mean temperature of the intermittent snowfall is −2.7°C. The ERA5 2-m temperatures are approximately 1°C colder than the surface observations for all three snowfall regimes.

Wind roses illustrate that the wind speed and direction differ for the snowfall regimes (Fig. 6). The frequency of wind directions is shown through concentric rings, colors illustrate the binned wind speed range and fractional occurrence, and the spokes show the direction of wind origin. Shallow snowfall (Fig. 6a) is dominated by two wind modes occurring from the east-southeast (ESE) 23% of the time with speeds ranging from 1 to 11 m s^{-1} and west-northwest (WNW) 20% of the time with speeds ranging from 1 to greater than 11 m s^{-1}. The deep and intermittent snowfall regimes have winds that are dominated by the southeast (SE) and west (W) directions, respectively (Figs. 6b,c). The two regimes have markedly different wind speeds, though. Deep snowfall is characterized by relatively lower wind speeds (3–9 m s^{-1}), whereas intermittent snowfall has wind speeds from 5 to greater than 11 m s^{-1}. In addition, wind gusts greater than 20 m s^{-1} were observed during the intermittent snowfall regime (figure not shown). The air advected from the North Atlantic and North Sea along W winds for the intermittent events flows through complex fjords and coastal mountains (Fig. 6c). Orographic interactions may explain the intermittent or pulsed nature of the snowfall observed in the strong updrafts of −1 m s^{-1} in the Doppler velocity, the large spectral width near the surface (>1 m s^{-1}) (Figs. 3h,i), and the large variance in PIP particle fall speeds with values greater than 2 m s^{-1} and upward motions as high as −0.5 m s^{-1} (Fig. 4b).

Distinctions between the snowfall regimes are further highlighted through different circulation patterns illustrated by composites means of MSLP and Z_{500}, and their corresponding mean anomalies (Fig. 7). In addition, the temperature and RH profiles for the snowfall regimes (Figs. 8a,b) are described in relation to the atmospheric circulation and microphysical characteristics, which are sensitive to moisture and temperature profiles (Libbrecht 2005; Ware et al. 2006). The MSLP and Z_{500} are generally high over the Scandinavian Peninsula (1020 hPa and 5430 m, respectively) during the shallow snowfall regime (Fig. 7a). Examination of the shallow snowfall events also shows that the ridge is persistent in time over the region for several events (figure not shown). The ridge is anomalously high in the MSLP (>+15 hPa) and the Z_{500} field over northern Scandinavia and the Barents Sea (+40–+180 m) (Fig. 7d). The temperature and RH inversion at 800 hPa correspond to the top of the shallow, stable boundary layer, and the air aloft is drier with the mean RH below 75% (Figs. 8a,b). Below 800 hPa, the temperature increases from −15° to −8°C. This suggests that the ice particles falling through the shallow boundary layer would be growing effectively through the dendritic growth zone (DGZ) (Hallett 1965).

The deep snowfall regime is associated with weak low pressure off the coast of Norway to the SW of the site (Fig. 7b). The weak low conditions correspond to slightly negative MSLP and Z_{500} anomalies (Fig. 7e). The synoptic disturbances advect moisture from the North Sea with SE surface winds and air parcels moving along gradual upslope toward the site and results in a moist RH profile throughout the boundary layer and free troposphere, with the mean RH exceeding 90% up to 400 hPa (Figs. 8a,b).

Intermittent snowfall in Haukeliseter is associated with strong low MSLP (980 hPa) along the western coast of Norway. The mean Z_{500} displays a trough, and the contours indicate a pattern of westerly geostrophic winds flowing directly over

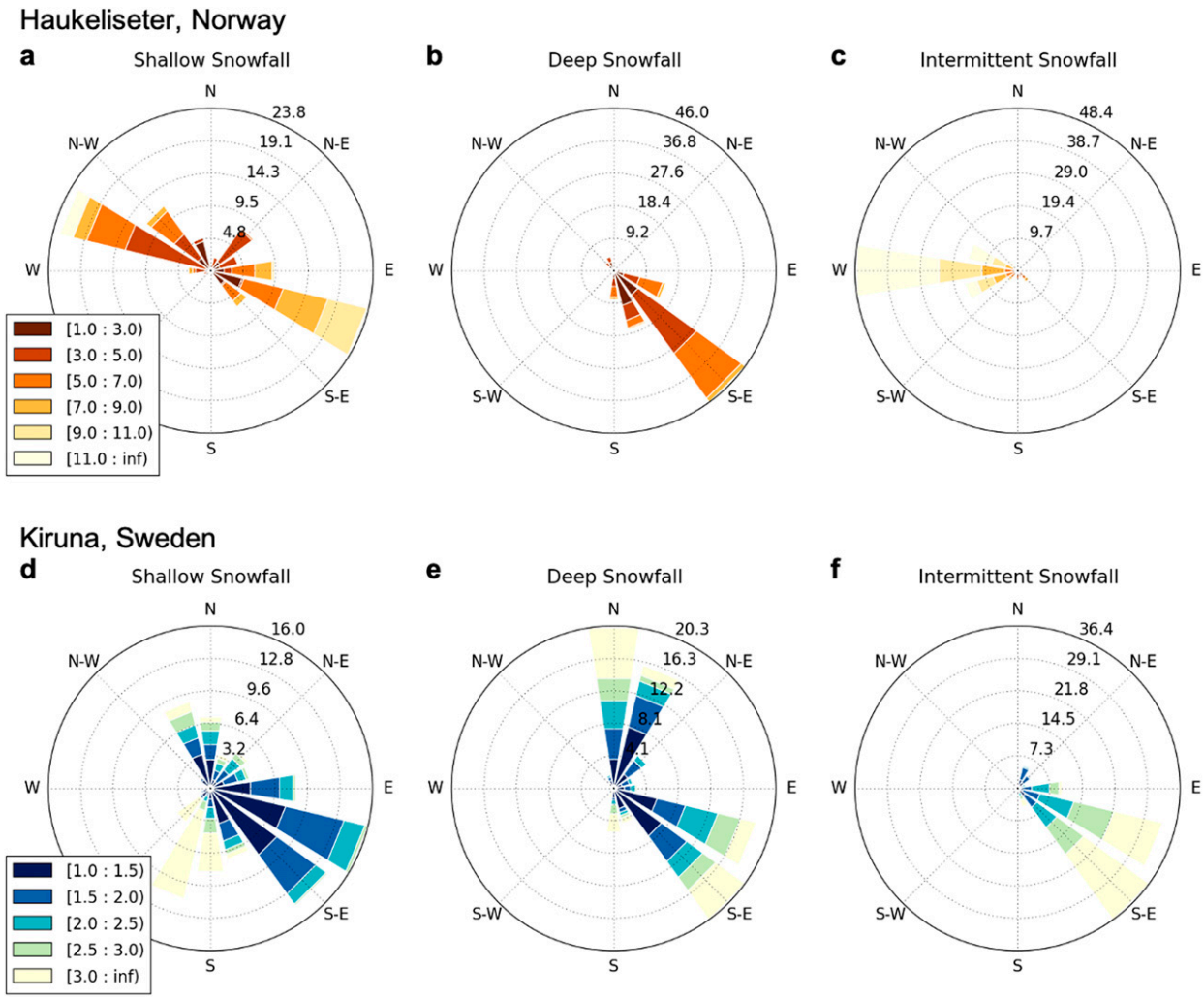

FIG. 6. Wind roses of the observed 10-m wind speed and direction at Haukeliseter during the distinct snowfall regimes: (a) shallow, (b) deep, and (c) intermittent. Also shown are wind roses for the observed surface winds at Kiruna during the snowfall regimes: (d) shallow, (e) deep, and (f) intermittent. The concentric rings are the frequency of occurrence, and the colors represent wind speed (values shown in the legends on the left). Spokes indicate the source direction of the wind.

southern Norway. The strong low pressure is associated with anomalously low MSLP (from −10 to −20 hPa) and also large negative Z_{500} anomalies (from −100 to −180 m) (Fig. 7f). The intermittent snowfall temperature profile is warmer than the shallow and deep profiles below 800 hPa, and between 450 and 775 hPa, the lapse rate is nearly constant at approximately 7.2°C km^{-1}, larger than the shallow and deep snowfall regime lapse rates (Fig. 8a). The free troposphere is drier in the mean RH for the intermittent snowfall regime than the deep regime; moisture for the intermittent regime is highest below 700 hPa with RH > 75% and increases toward the surface where there is a maximum (95%) at 800 hPa (Fig. 8b).

b. Kiruna

At the Kiruna site, shallow snowfall dominates the precipitation occurrence with a total of 25 events and 486 h (Table 1). Deep snowfall events are also frequently observed (23 events), but the duration is shorter resulting in 180 total hours. The intermittent snowfall regime in Kiruna is uncommon during the deployment and only three events were identified. While the shallow snowfall occurs most frequently, it contributes the least to snowfall accumulation (see event accumulations in the appendix) with lowest mean snowfall rates ranging from 0.07 to 0.15 mm h^{-1} for the retrievals and PIP-observed LWE (Table 1). The deep and intermittent snowfall regimes are similar with moderate mean rates in Kiruna; deep snowfall mean rates range between 0.33 and 0.52 mm h^{-1}, and intermittent snowfall mean rates range between 0.39 and 0.64 mm h^{-1} (Table 1). Although the intermittent snowfall has the lowest occurrence frequency, the event duration coupled with the moderate mean snowfall rates results in substantial snowfall accumulation per event.

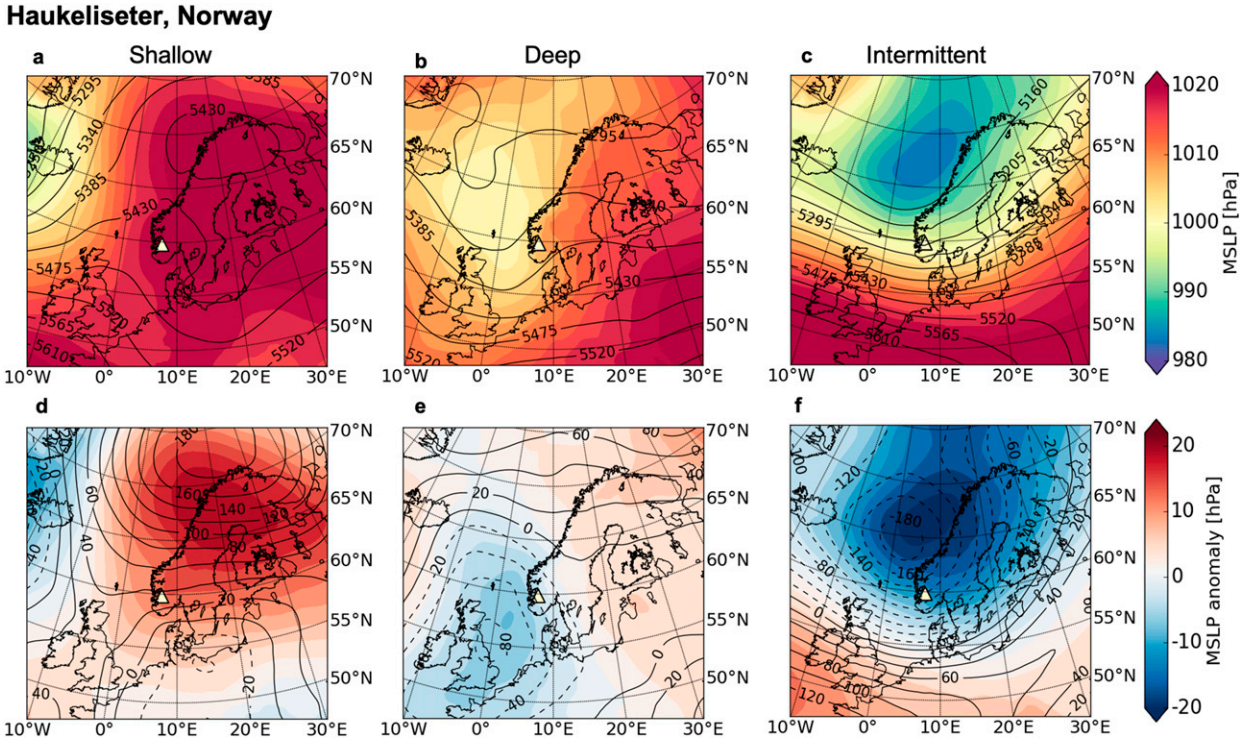

FIG. 7. Composites of mean MSLP and Z_{500}, and corresponding anomalies for snowfall regimes in Haukeliseter. Shown are composites of mean MSLP (color shading) and Z_{500} (black contour lines) for the (a) shallow, (b) deep, and (c) intermittent regimes and mean MSLP anomalies (color shading) and Z_{500} anomalies (black contour lines) for the (d) shallow, (e) deep, and (f) intermittent regimes The anomalies are calculated from the 1979–2018 monthly climatology.

1) SNOWFALL CHARACTERISTICS

The 2D histograms of MRR profiles for reflectivity, Doppler velocity, and spectral width reveal distinct characteristics for the shallow, deep, and intermittent snowfall regimes in Kiruna (Fig. 9). The shallow snowfall has precipitation echo-top heights mostly below 1.5 km AGL (Fig. 9a) with a narrow range of reflectivity from 0 to 5 dBZ. At 0.5 km AGL, reflectivity is broad between −5 and 10 dBZ, with a maximum of 15 dBZ. The corresponding Doppler velocity profile ranges from 0.5 to 1 m s^{-1} at 1.5 km AGL and broadens toward 0.5 km AGL with values between 0.25 and 1 m s^{-1} (Fig. 9b). The spectral width values at the precipitation echo-top height are 0.2 m s^{-1} and increase slightly to 0.45 m s^{-1} at 0.5 km AGL (Fig. 9c). While the shallow snowfall regime observed in Kiruna does not appear to have turbulent motions like Haukeliseter in the shallow column of precipitation, individual cases do contain upward Doppler velocities with a lower magnitude and less frequently (figure not shown).

For the deep snowfall regime, the MRR profile of radar reflectivity increases with decreasing height (Fig. 9d), which is consistent with deep snowfall in Haukeliseter. At the MRR height limit of 3 km AGL, the reflectivities range from 0 to 10 dBZ, and the maximum MRR reflectivity approaches 17 dBZ at 0.5 km AGL. The 2D histogram further reveals two local count maxima of increasing reflectivity within the spread of values. One of the maxima starts near 5 dBZ at 3km AGL and increases to 15 dBZ at 0.5 km AGL. The second maxima begins with 0 dBZ at 1.75 km AGL and increases to 10 dBZ at 0.5 km AGL. The Doppler velocity (Fig. 9e) and spectral width (Fig. 9f) are nearly constant throughout the column with approximate values 1 and 0.2 m s^{-1}, respectively; and the profiles do not contain updrafts or increases in spectral width throughout the column, which were present in the Haukeliseter deep snowfall composites.

The MRR reflectivity for the intermittent snowfall regime has the broadest range of the three regimes in Kiruna (Fig. 9g). At 3 km AGL, the reflectivity values fall between 0 and 10 dBZ, but at 0.5 km AGL, the range expands to include from −5 to 20 dBZ. The highest concentration of Doppler velocity observations occurs below 2 km AGL (Fig. 9h), and the Doppler velocity values increase from 0.8 m s^{-1} at 1.5 km AGL to 1.5 m s^{-1} at 0.5 km AGL. This is unlike profile in Haukeliseter, which shows decreasing Doppler velocity toward the surface possibly due to turbulent motions associated with the complex terrain. Throughout the column, the spectral width has minimal variability (between 0.2 and 0.3 m s^{-1}) but begins to have increasing values below 1.5 km AGL, and at 0.5 km AGL the spread of the spectral width is much larger (>0.6 m s^{-1}) than the spectral width of the shallow and deep snowfall regime (Fig. 9i), and the increase

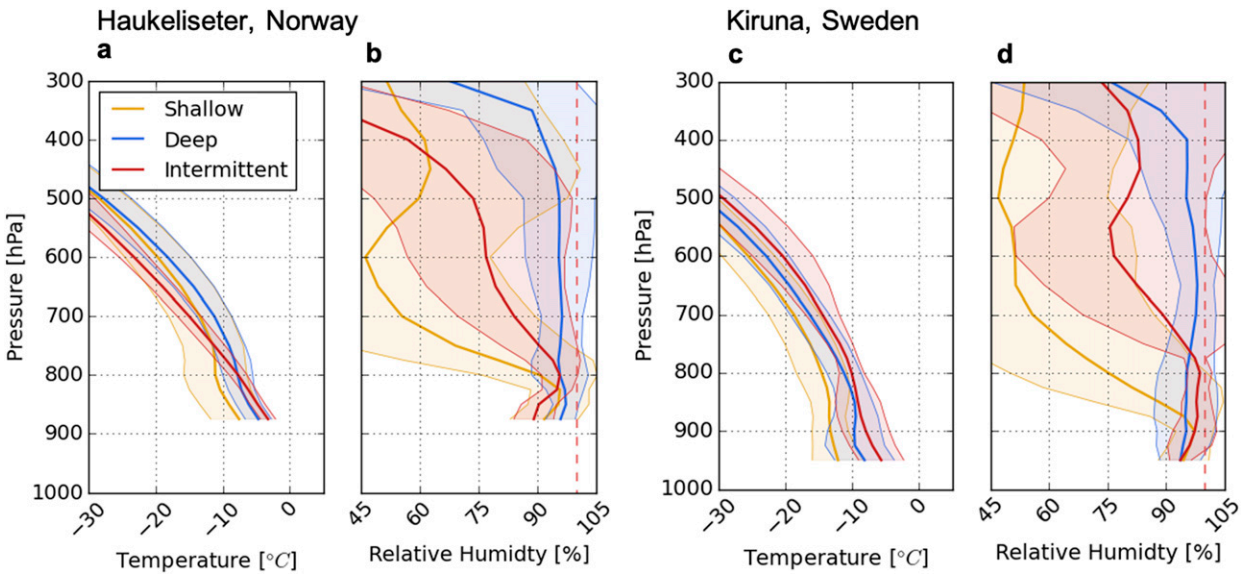

FIG. 8. Vertical profiles of (a),(c) temperature and (b),(d) relative humidity at (left) Haukeliseter and (right) Kiruna for the shallow, deep, and intermittent regimes. The solid lines are the averages for the regimes, and the shaded envelopes indicate 1 standard deviation above and below the average. The red dashed line in (b) and (d) is the 100% relativity line illustrating saturation with respect to liquid water. The lowest pressure level/surface pressure was approximated from the winter average sea level pressure. Average sea level pressure is 875 hPa at Haukeliseter and 950 hPa at Kiruna.

toward the surface is similar to the intermittent snowfall in Haukeliseter but is not as large in magnitude.

Similar to Haukeliseter, the PIP-derived mean PSDs and fall speeds show distinct microphysical characteristics for the three regimes (Figs. 4c,d). The shallow snowfall regime mean PSD has a lower concentration of particles than do the deep and intermittent regimes. The mean PSD for the deep regime is narrow and dominated by small particles. The intermittent regime has higher particle concentration for $D > 2$ mm relative to the other regimes. Shallow snowfall has the lowest mean fall speeds, which increase from $0.5\,\mathrm{m\,s^{-1}}$ for particles of $D < 0.4$ mm to $1.25\,\mathrm{m\,s^{-1}}$ for particles of $D > 7$ mm. The mean fall speeds for deep and intermittent snowfall are both $0.75\,\mathrm{m\,s^{-1}}$ for small particles ($D < 0.4$ mm), and both gradually increase to greater than $1.5\,\mathrm{m\,s^{-1}}$. For the intermittent snowfall regime, some fall speeds exceed $2\,\mathrm{m\,s^{-1}}$ for particles $D > 7$ mm indicated by the spread of fall speeds within 1 standard deviation from the mean.

2) METEOROLOGICAL OBSERVATIONS AND ATMOSPHERIC CIRCULATION

Winter months in Kiruna are colder than in Haukeliseter (Fig. 5). In general, December, January, and February have the lowest mean winter temperatures, and the largest range of temperatures, from −35° to −5°C. The mean ERA5 2-m temperatures for November, December, and January during the deployment period (2017–18) are close to the indicated climatological mean. The mean temperatures during February and March 2018 were colder than climatology by 2°C but within the interquartile range. The deployment mean for April 2018 was slightly warmer than the mean climatology, but also within the interquartile range.

Similar to Haukeliseter, the observed surface temperature distributions are unique for snowfall regimes (Fig. 5b). Shallow snowfall is associated with lower temperatures; the observed mean is −13.7°C, and the range spans as low as −28°C. Deep snowfall occurs under warmer conditions and a narrower temperature range, with an observed mean of −9.7°C. The temperature distribution for intermittent snowfall is the narrowest and warmest of the snowfall regimes. The observed mean surface temperature is −6.1°C. The ERA5 2-m mean temperatures are approximately 1°C warmer than the surface observations.

In general, Kiruna is dominated by lower wind speeds during precipitation events relative to Haukeliseter (note the color bar in Figs. 6d–f). Shallow snowfall regime winds are diffuse between the north (N), SE, south (S), and south-southwest (SSW) directions (Fig. 6d). Winds from the S and southwest (SW) have the highest wind speeds, with a maximum of $9.5\,\mathrm{m\,s^{-1}}$. The SE and ESE winds have lower wind speeds between 1 and $2.4\,\mathrm{m\,s^{-1}}$ occurring approximately 30% of the time. The deep snowfall regime is characterized by two general wind modes: N and ESE (Fig. 6e) and wind speeds mostly between 1 and $3\,\mathrm{m\,s^{-1}}$. Figure 6f shows that the intermittent snowfall is dominated by SE winds that occur nearly 70% of intermittent snowfall. Similar to Haukeliseter, the wind speeds associated with intermittent snowfall are higher at Kiruna than the shallow and deep snowfall regimes with most measurements greater than $3\,\mathrm{m\,s^{-1}}$, and a maximum wind speed of $6.4\,\mathrm{m\,s^{-1}}$.

The mean composites of MSLP, Z_{500}, their respective anomalies (Fig. 10), and the thermodynamic profiles of temperature and RH (Figs. 8c,d) help to further illuminate the conditions for the shallow, deep, and intermittent snowfall

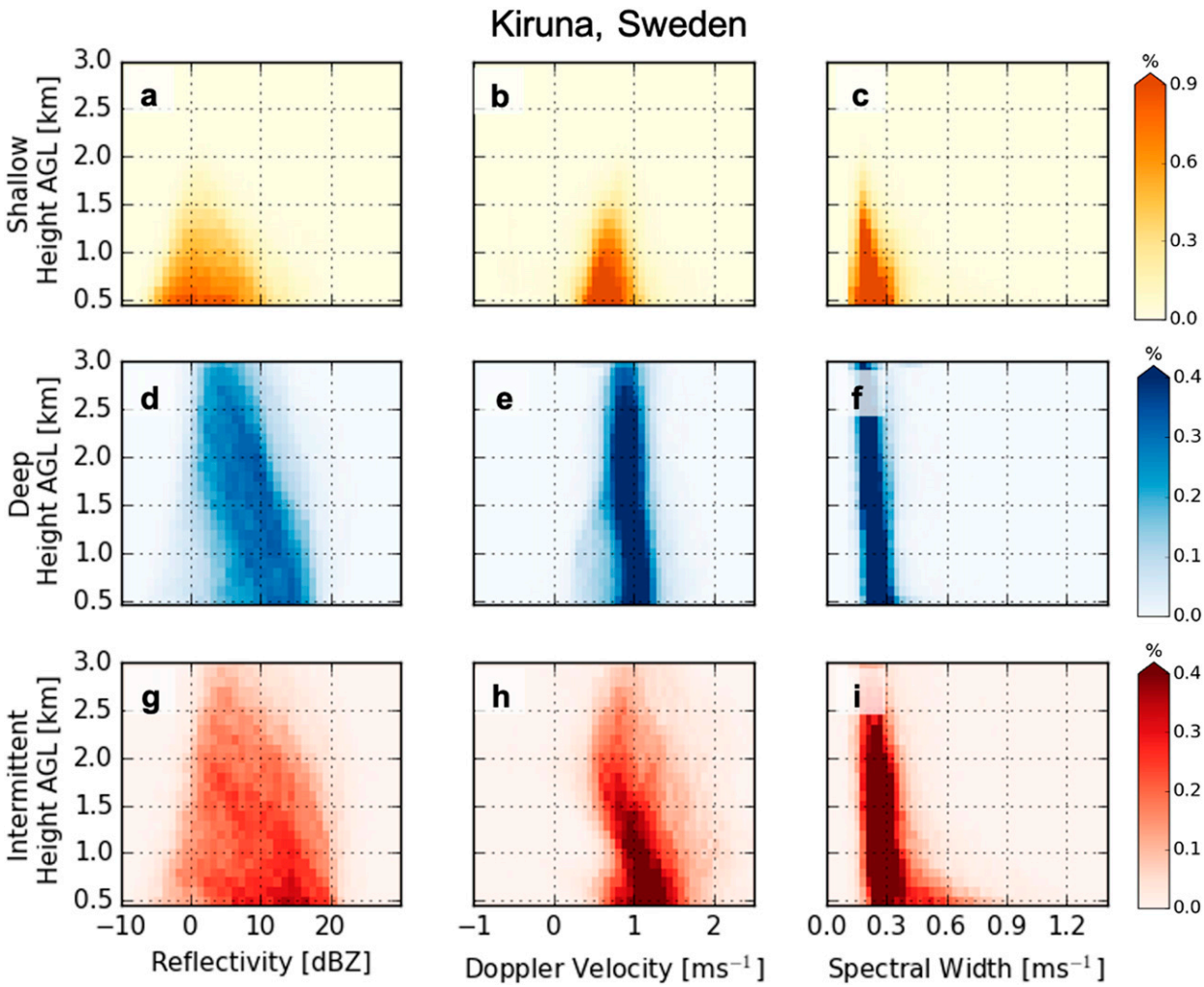

FIG. 9. As in Fig. 3, but for Kiruna.

regimes in Kiruna. Shallow snowfall is associated with high MSLP values (1015 hPa at the site) over northern Scandinavia, and in many events the high pressure was persistent in time over this area during the events (figure not shown). Unlike shallow snowfall in Haukeliseter, the MSLP anomalies are only slightly positive over the region (+5 hPa), and the Z_{500} field is not anomalous over Kiruna (0 m). The ridge over Scandinavia results in a stable, cold temperature profile at the site with an inversion at 875 hPa (Fig. 8c). The top of the boundary layer has a maximum RH of 95% at 900 hPa before decreasing throughout the free troposphere (Fig. 8d). From 800 hPa to the surface, the mean temperature increases slightly from −15° to −12°C, which is within the DGZ and similar to the mean temperature profile for Haukeliseter shallow snowfall.

The deep snowfall regime is associated with a mean MSLP of approximately 1000 hPa over Scandinavia and the Norwegian Sea (Fig. 10b). In the anomaly field, the MSLP and the Z_{500} are slightly negative over Scandinavia and northern Europe (Fig. 10e). Through the height of the boundary layer and free troposphere, the snowfall regime temperature profile is generally warmer than the shallow regime, and colder than the intermittent snowfall regime. It is also nearly isothermal from 900 to 850 hPa with a mean temperature of −10°C (Fig. 8c). The RH is high (>90%) throughout the boundary layer and free troposphere up to 500 hPa, which indicates abundant available moisture for snowfall to form and fall from deep clouds.

Similar to intermittent snowfall in Haukeliseter, Fig. 10c shows that the intermittent snowfall regime in Kiruna is also characterized by a strong low MSLP (<980 hPa) along the coast of Norway. The low pressure corresponds to large negative MSLP and Z_{500} anomalies (−20 hPa and −200 m, respectively) at the center of the low (Fig. 10f). This strong low brings the warm, moist air to the site, illustrated by the vertical temperature profile that is warmer than that of shallow and deep snowfall (Fig. 8c), and the RH profile shows that it is most moist closer to the surface between 800 and 900 hPa (RH of 98%) (Fig. 8d), similar also to intermittent snowfall in Haukeliseter.

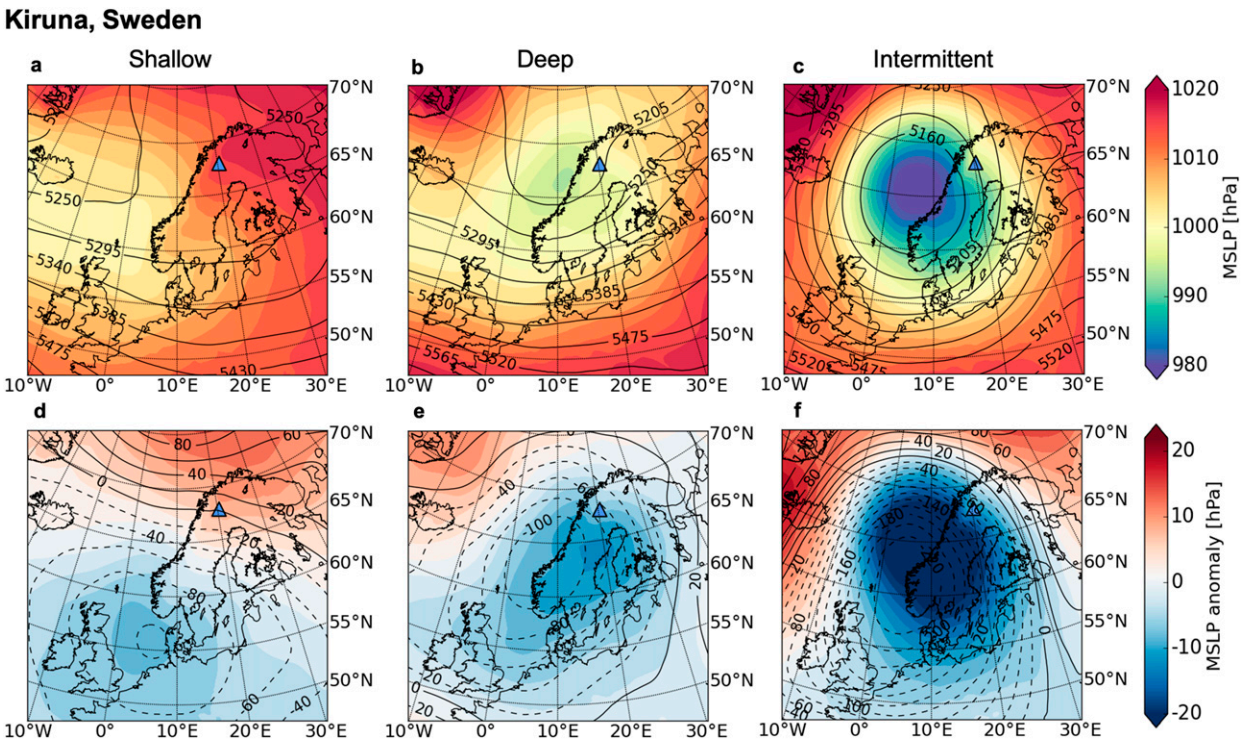

FIG. 10. As in Fig. 7, but for Kiruna.

5. Discussion

a. Shallow snowfall

The shallow snowfall regime generally occurs under conditions of cold surface temperatures, high MSLP and a moist shallow boundary layer with dry air aloft (Figs. 5b, 7, 8b,d, 10). In Haukeliseter, the ridging pattern was highly anomalous, but in Kiruna, it was not anomalous, and the shallow snowfall regime was common during the 2017/18 winter deployment. At the surface for both sites, the shallow snowfall produces light LWE rates (Table 1), the radar reflectivity values are relatively low and broad (from −5 to 15 dBZ) (Figs. 3a, 9a) and the snowflake particle concentrations are lower at all particle diameters than the other two regimes (Figs. 4a,c). The boundary layer temperatures in the DGZ favor efficient snowfall production (Hallett 1965), and the decreasing RH toward the surface (Figs. 8b,d) is similar to boundary layer conditions in LeS (Barthold and Kristovich 2011; Pettersen et al. 2020a). The decrease in RH may potentially suggest sublimation of smaller particles and result in lower concentrations of small particles in the PIP PSDs (Figs. 4a,c). The most frequently observed wind direction at both sites for the shallow snowfall was from the SE (Figs. 6a,d), which corresponds to mean anticyclonic circulation and colder and drier continental air advecting toward the sites (Figs. 7 and 10). The shallow snowfall regime shares characteristics with other shallow snowfall producing clouds. The low precipitation echo tops and variability in radar reflectivity values found in the shallow snowfall regime are consistent with shallow mixed-phase stratus clouds (Shupe et al. 2008) and shallow convective boundary layer clouds (Wang et al. 2016) observed in the North Slope of Alaska, shallow mixed phase clouds at Summit Station in Greenland (Pettersen et al. 2018), and shallow and near surface convective snowfall in the Pyeongchang area in South Korea (Jeoung et al. 2020). In addition, the synoptic conditions are consistent with shallow mixed-phase stratus, which often occurs with persistent, large-scale subsidence in the Arctic (Verlinde et al. 2007; Morrison et al. 2012; Pettersen et al. 2018; McIlhattan et al. 2020). The shallow snowfall regime conditions are also consistent with LeS, which propagate well under cold air outbreaks and high MSLP (Eichenlaub 1970; Kristovich et al. 2017; Pettersen et al. 2020a). Near surface and shallow snowfall in South Korea has also been connected with cold air mass outbreaks (Jeoung et al. 2020).

The topographic features around the Haukeliseter site contributed to unique characteristics in the shallow snowfall that differed from Kiruna. SE winds in the shallow snowfall regime in Haukeliseter indicate upslope movement along a relatively gentle rise from sea level, while the W winds correspond to air moving around complex terrain (Figs. 6a and 1), which differs drastically from the relatively flat topography around Kiruna. The upward motions detected in the Doppler velocity values and the relatively large spectral width (Figs. 3b,c) suggests presence of turbulent motions (Matrosov et al. 2008). The turbulent nature of the precipitation and low-level echo tops of the shallow snowfall regime at Haukeliseter shares characteristics seen in LeS. Although the mechanisms for turbulence may not be the same, MRR Doppler velocities

observed during LeS events in Marquette, Michigan, revealed updrafts within the moist, shallow boundary layer (Pettersen et al. 2020a), which is consistent with our results of shallow snowfall in mountainous terrain. The convective characteristics in the shallow snowfall in Kiruna occurred at a lower magnitude than at Haukeliseter but are observable in individual cases in the MRR Doppler velocity and time series of reflectivity (Fig. 2a). The Doppler velocity and reflectivity profiles are consistent with the shallow convective snowfall in the North Slope of Alaska (Wang et al. 2016) and in the Pyeongchang area in South Korea (Jeoung et al. 2020).

b. Deep snowfall

The deep snowfall regime is associated with weakly anomalous low MSLP, and moderate, continuous snowfall. Kulie et al. (2016) showed that deep nimbostratus clouds are responsible for over 75% of annual snowfall accumulation over Scandinavia and over 50% of the snowfall fraction by occurrence, which relates to the deep snowfall regime in that the ERA5 reanalysis thermodynamic profiles revealed that the atmosphere is moist from the surface through the free troposphere, indicating snowfall forming and falling from relatively deep clouds. Radar reflectivity increases toward the surface (Figs. 3d and 9d), which likely indicates particle growth by aggregation (Field 2000). In Kiruna, the Doppler velocity and spectral width are relatively invariant with height remaining approximately $1\,\mathrm{m\,s^{-1}}$ indicating no updrafts below 3 km AGL (Figs. 9e,f). In contrast, the MRR observations in Haukeliseter indicate a spread in spectral width and some upward motions in the column, which could also suggest particle growth by riming and aggregation from orographic induced turbulence (Houze and Medina 2005). Snowflake imagery from a Multi-Angle Snowflake Camera during a deep (upslope) snowfall event in Haukeliseter confirms riming and aggregation of particles (Schirle et al. 2019). At both sites, the PIP PSDs are relatively narrow and dominated by smaller particles (Figs. 4a,c). The general features of the thermodynamic profiles, PIP PSDs, and MRR composites are consistent with deep, synoptically driven snowfall observed in Marquette (Pettersen et al. 2020a). The thermodynamic profiles and radar reflectivity values are also reminiscent of characteristics observed in winter storms along the East Coast of the United States (Stark et al. 2013).

c. Intermittent snowfall

The intermittent snowfall regime results from intense, anomalous low pressure systems along the coast of Norway. The surface temperatures associated with the intermittent snowfall regime were the warmest, winds speeds were consistently higher, and the snowfall rates were the highest of the three regimes. Examination of individual events (not shown) revealed that some intermittent snowfall events also correspond to elevated amounts of total column water vapor that extended to the sites and northern Europe as filamentary plumes from lower latitudes. The intermittent snowfall regime RH profile is distinct from the deep snowfall regime in that the RH is high near the surface and drier aloft (Figs. 8b,d).

TABLE A1. Event list for shallow snowfall events in Haukeliseter. The two columns for each of Z_e–S, S19b6, S19b8, PIP, and DFAR show the mean LWE rates and the event accumulations respectively. The LWE rate for the PIP is specifically for nonrain precipitation. The mean event temperatures are listed for temperature ("temp"). The winds include the mode of the wind direction and the mean wind speed for the event. The X symbol indicates missing observations for the event.

Start hour (UTC)	End hour (UTC)	Z_e–S ($\mathrm{mm\,h^{-1}}$)	Z_e–S (mm)	S19b6 ($\mathrm{mm\,h^{-1}}$)	S19b6 (mm)	S19b8 ($\mathrm{mm\,h^{-1}}$)	S19b8 (mm)	PIP ($\mathrm{mm\,h^{-1}}$)	PIP (mm)	DFAR ($\mathrm{mm\,h^{-1}}$)	DFAR (mm)	Temp (°C)	Winds ($\mathrm{m\,s^{-1}}$)
1900 5 Nov	0200 6 Nov	0.18	1.2	0.11	0.71	0.18	1.15	X	X	0.23	0.42	−6.04	ESE 7.5
0200 9 Nov	1200 10 Nov	0.07	1.3	0.06	1.06	0.08	1.55	X	X	0.05	0.55	−11.8	NNE 1.97
1400 24 Nov	1800 24 Nov	0.2	0.7	0.12	0.44	0.2	0.74	X	X	0.19	0.19	0.65	ESE 1.9
1400 26 Nov	1600 26 Nov	0.13	0.15	0.06	0.7	0.11	0.12	X	X	0.35	0.37	−1.3	WNW 14.5
1200 5 Dec	1500 5 Dec	0.06	0.09	0.04	0.04	0.05	0.07	X	X	X	X	0.62	WNW 6.6
0600 29 Dec	0000 30 Dec	0.07	0.4	0.04	0.2	0.06	0.33	0.08	0.41	0.1	0.1	0.69	W 4.7
0300 6 Feb	1000 7 Feb	0.21	5.3	0.13	2.04	0.2	3.23	0.08	0.23	X	X	−8.22	X
1800 13 Apr	2000 13 April	0.07	0.11	X	X	X	X	X	X	0.22	0.2	−2.9	WNW 6.8
1300 18 Apr	0300 19 April	0.08	0.7	X	X	X	X	X	X	0.08	0.38	−2.97	WNW 3.5
1200 28 Apr	0800 29 April	0.35	6.1	X	X	X	X	X	X	0.21	2.7	−1.94	ESE 7.4

TABLE A2. As in Table A1, but for deep snowfall events in Haukeliseter.

Start hour (UTC)	End hour (UTC)	Z_e–S (mm h^{-1})	Z_e–S (mm)	S19b6 (mm h^{-1})	S19b6 (mm)	S19b8 (mm h^{-1})	S19b8 (mm)	PIP (mm h^{-1})	PIP (mm)	DFAR (mm h^{-1})	DFAR (mm)	Temp (°C)	Winds (m s^{-1})
1800 4 Nov	1800 5 Nov	1.05	25.2	0.89	21.4	1.52	36.0	X	X	0.59	13.67	−5.06	SE 4.9
1200 12 Nov	2300 12 Nov	0.6	6.5	0.46	4.78	0.76	7.92	X	X	0.36	3.43	−1.5	SE 3.3
0700 18 Nov	1200 18 Nov	0.55	2.7	0.43	2.15	0.73	3.7	X	X	0.48	2.19	−2.55	E 1.59
1600 19 Nov	2100 19 Nov	0.61	2.7	0.5	2.13	0.82	3.6	PIP	PIP	X	X	−4.26	X
1200 20 Nov	1600 20 Nov	1.14	4.6	1.0	4.02	1.7	6.82	X	X	X	X	−3.62	X
0000 21 Nov	0200 21 Nov	0.33	0.7	0.22	0.44	0.38	0.75	X	X	X	X	−2.38	X
1000 1 Dec	1100 1 Dec	0.4	0.4	0.23	0.24	0.4	0.4	X	X	X	X	1.13	X
1600 23 Dec	2100 23 Dec	1.9	9.13	1.73	8.36	2.95	14.3	X	X	2.1	9	−0.59	S 5.63
0900 6 Jan	1600 6 Jan	0.4	2.7	0.3	1.8	0.45	2.7	X	X	0.24	1.53	−4.32	SE 2
2000 9 Jan	0200 10 Jan	1.11	6.4	0.9	4.95	1.5	8.5	0.15	0.28	0.42	2.11	−0.06	SE 6
0600 13 Jan	0800 13 Jan	0.6	1.07	0.5	0.88	0.77	1.47	0.4	0.63	0.52	0.8	−6.03	SSE 2.42
1500 28 Jan	1600 28 Jan	0.5	0.45	0.37	0.35	0.6	0.58	PIP	PIP	X	X	−5.75	SE 5
0800 2 Feb	1500 2 Feb	1.1	7.5	0.99	6.6	1.7	10.8	X	X	X	X	−4.55	ESE 3.88
1200 3 Feb	1700 3 Feb	1.03	5.13	0.9	4.87	1.55	6.89	0.94	5.6	X	X	−4.32	SSE 1
1600 4 Feb	2200 4 Feb	0.6	3.4	0.5	2.78	0.82	4.55	0.2	0.46	X	X	−5.42	ESE 3.3
1500 11 April	1800 11 April	0.66	2.0	X	X	X	X	X	X	0.9	2.11	−2.7	SSE 2
0200 15 April	0600 15 April	0.52	2.1	X	X	X	X	X	X	0.54	1.9	−5.35	SE 5.1
0900 16 April	1000 16 April	1.32	1.33	X	X	X	X	PIP	PIP	0.93	0.5	−2.45	SSE 2.7
0000 27 April	0400 27 April	0.24	0.95	X	X	X	X	PIP	PIP	0.24	0.84	−4.9	NNW 3.3

In Haukeliseter, the MRR and PIP observations support the occurrence of updrafts in excess of 0.5 m s^{-1} in the intermittent regime (Figs. 3h,i and 4b). The turbulent motions at the surface and above the radar from the complex terrain may result in the presence of supercooled cloud liquid water and accretion onto the ice particles (Houze and Medina 2005) leading to high radar reflectivity values ($Z_e > 25$ dBZ) and high snowfall rates. In addition, graupel particles and rimed aggregates were captured by a Multi-Angle Snowflake Camera by Schirle et al. (2019) during an intermittent ("pulsed") event. Unlike Haukeliseter, the terrain surrounding Kiruna has little elevation change, and no observable updrafts, but at 1.5 km AGL, the MRR contains an increase in Doppler velocity and spectral width toward the surface. The increase in spectral width suggests the presence of some boundary layer turbulence, which can result in supersaturations and the formation of supercooled droplets. The increase in Doppler velocity toward the surface may indicate riming as a growth mechanism (Mosimann 1995; Stark et al. 2013; Kneifel and Moisseev 2020).

6. Conclusions

By leveraging observations and reanalysis products at two separate sites in Scandinavia—Haukeliseter, Norway, and Kiruna, Sweden—we gain an understanding of the roles of synoptic-scale circulations and regional topography on snowfall processes. We characterized and investigated three specific snowfall regimes—shallow, deep, and intermittent—and used MRR, PIP, surface meteorological observations, and ERA5 reanalysis products to compare and contrast the snowfall characteristics and environmental conditions at the two sites.

Shallow snowfall is generally long-lived, produces light snowfall, and occurs under regions of high pressure and large-scale subsidence. The deep snowfall regime produces moderate snowfall rates under relatively weak synoptic disturbances. The intermittent snowfall regime is associated with high impact snowfall and occurs during warm and moist conditions associated with strong extratropical cyclones. Snowfall in Haukeliseter is enhanced by local complex topography for all three regimes, and the MRR and PIP observations suggest evidence of turbulence in the column.

In addition to comparing the shallow, deep, and intermittent snowfall regimes between the two sites, this study adds to the existing body of knowledge on snowfall across the mid- and high latitudes. The shallow snowfall regime shares characteristics with other shallow types of snowfall such as lake-effect snow and precipitating Arctic mixed phase clouds (Pettersen et al. 2018, 2020a). The deep and intermittent snowfall are driven by low pressure systems and occur with deeper clouds. The intermittent snowfall regime is higher impact and associated with extratropical cyclones, some of which may be associated with atmospheric river events.

The measurements at Haukeliseter and Kiruna are valuable for future validation studies. The shallow snowfall regime highlights the frequency of occurrence of snowfall with shallow precipitation echo tops (<1.5 km AGL) that may be missed entirely by satellite observations due to blind zone limitations. Additionally, snowfall over complex terrain is difficult to

TABLE A3. As in Table A1, but for intermittent snowfall events in Haukeliseter.

Start hour (UTC)	End hour (UTC)	Z_e–S (mm h^{-1})	Z_e–S (mm)	S19b6 (mm h^{-1})	S19b6 (mm)	S19b8 (mm h^{-1})	S19b8 (mm)	PIP (mm h^{-1})	PIP (mm)	DFAR (mm h^{-1})	DFAR (mm)	Temp (°C)	Winds (m s^{-1})
1600 16 Nov	1500 17 Nov	1.1	22.1	0.97	19.3	1.62	32.7	X	X	0.83	22.3	−1.9	SW 5.4
0900 21 Dec	0800 23 Dec	1.7	64.4	1.56	57.6	2.56	91.5	0.85	5.32	1.02	46	−2.10	W 8.8
0000 24 Dec	0500 25 Dec	1.47	37.8	1.32	33.2	2.2	55.95	X	X	0.8	22.12	−3.42	W 10.6
0000 26 Dec	1800 26 Dec	1.56	24.3	1.33	20.5	2.26	32.8	4.8	45.1	1.02	17.4	−3.51	W 13.4
0600 3 Jan	2300 3 Jan	0.62	6.8	0.5	5.3	0.83	9	0.2	1.1	0.48	6.8	−3.40	WNW 11.2
0400 10 Jan	0000 11 Jan	0.97	14.2	0.85	11.96	1.44	19.5	0.15	0.96	0.44	7.15	−1.66	SE 5.2
2000 11 Jan	0000 13 Jan	1.1	24.64	0.89	19.8	1.5	33.45	7.46	47.4	0.8	21.5	−4.42	W 10.3
0100 9 Mar	1800 9 Mar	0.63	7.5	0.51	5.9	0.84	9.8	0.95	8.2	0.5	7.1	−3.13	WSW 9.1
1400 14 Mar	1900 15 Mar	0.96	24.4	1.03	8.96	1.75	15.3	X	X	X	X	−2.15	X
0000 17 Mar	1700 17 Mar	1.3	16.7	1.2	15.12	2.0	25.6	2.35	25.1	X	X	−3.72	X
1400 20 Mar	0900 21 Mar	1.43	20.3	1.3	17.6	2.1	29.8	X	X	X	X	−1.93	X
2100 4 Apr	1100 5 Apr	1.21	15.7	X	X	X	X	X	X	0.8	10.6	−1.9	W 13.3
0300 21 Apr	1800 21 Apr	0.86	10.78	X	X	X	X	X	X	0.65	8.44	−2.17	W 11.25

TABLE A4. As in Table A1, but for shallow snowfall events in Kiruna.

Start hour (UTC)	End hour (UTC)	Z_e–S (mm h^{-1})	Z_e–S (mm)	S19b6 (mm h^{-1})	S19b6 (mm)	S19b8 (mm h^{-1})	S19b8 (mm)	PIP (mm h^{-1})	PIP (mm)	Temp (°C)	Winds (m s^{-1})
1200 18 Nov	0500 19 Nov	0.15	1.5	0.15	1.2	0.22	2	0.16	0.9	−7.1	N 0.5
0700 20 Nov	1600 20 Nov	0.68	6.16	0.5	4.6	0.85	7.62	0.3	2.6	−8.15	NE 2
2300 21 Nov	1800 22 Nov	0.13	1.85	0.11	1.5	0.17	2.34	0.05	0.64	−12.3	SE 0.66
0800 11 Dec	1000 11 Dec	0.17	0.28	0.12	0.2	0.2	0.33	0.07	0.11	−5.8	SE 0.48
0800 15 Dec	0000 16 Dec	0.1	1.31	0.08	1.0	0.12	1.54	0.05	0.32	−10.13	SW 0.48
2100 14 Jan	1400 15 Jan	0.18	2.9	0.14	0.43	0.22	0.67	0.07	1.17	−8.19	SSW 5.3
1200 20 Jan	0900 22 Jan	0.07	2.28	0.08	2.6	0.1	3.3	0.03	0.6	−18.77	SE 0.52
2200 27 Jan	0600 28 Jan	0.04	0.16	0.04	0.16	0.04	0.18	0.02	0.02	−20.4	ESE 1
2100 30 Jan	0800 3 Feb	0.1	4.62	0.09	4.53	0.12	6.16	0.03	0.57	−18	ESE 0.87
0000 7 Feb	0600 7 Feb	0.17	0.86	0.16	0.8	0.2	1.15	0.05	0.14	−17.63	SE 0.77
0500 11 Feb	1100 13 Feb	0.1	3.8	0.09	3	0.13	4.52	0.04	0.75	−10.07	S 1.9
1100 14 Feb	1800 14 Feb	0.04	0.08	0.02	0.04	0.03	0.07	0.03	0.07	−4.18	SSW 2.69
1800 17 Feb	0100 19 Feb	0.08	2.12	0.09	2.3	0.11	3.08	0.02	0.28	−17.07	NNW 0.57
0400 20 Feb	0800 20 Feb	0.04	0.16	0.04	0.15	0.05	0.2	0.02	0.05	−17.25	SSW 0.33
2000 22 Feb	1500 23 Feb	0.1	1.13	0.09	1	0.13	1.4	0.04	0.27	−13.23	N 1
2300 26 Feb	0900 27 Feb	0.03	0.16	0.03	0.11	0.03	0.15	0.03	X	−11.22	SE 0.47
1500 3 Mar	1100 4 Mar	0.17	3.27	0.14	2.6	0.2	4.05	0.14	2.7	−11.13	ESE 1.5
1500 6 Mar	1800 7 Mar	0.05	1.12	0.05	1.1	0.06	1.4	0.06	1.1	−17.98	ESE 0.83
1500 8 Mar	0000 10 Mar	0.05	1.24	0.06	1.3	0.07	1.6	0.01	0.02	−16.33	NNW 0.43
0000 11 Mar	0800 11 Mar	0.1	0.57	0.08	0.47	0.12	0.7	0.02	0.06	−11.46	NW 0.55
0900 13 Mar	0700 14 Mar	0.23	4.66	0.18	3.4	0.28	5.42	0.12	1.7	−10.42	NNW 2.2
0500 22 Mar	1000 22 Mar	0.1	0.3	0.06	0.17	0.1	0.27	0.04	0.05	−7.43	NE 2.44
0200 24 Mar	1500 24 Mar	0.08	1.1	0.6	0.73	0.09	1.07	0.04	0.2	−10.8	NNW 1.1
1800 9 Apr	2000 9 Apr	0.12	0.16	0.07	0.08	0.10	0.13	0.06	0.04	−1.9	NNW 3.27
0500 29 Apr	1300 29 Apr	0.07	0.33	0.07	0.2	0.09	0.4	0.16	0.85	−0.45	ENE 2.1

TABLE A5. As in Table A1, but for deep snowfall events in Kiruna.

Start hour (UTC)	End hour (UTC)	Z_e–S (mm h^{-1})	Z_e–S (mm)	S19b6 (mm h^{-1})	S19b6 (mm)	S19b8 (mm h^{-1})	S19b8 (mm)	PIP (mm h^{-1})	PIP (mm)	Temp (°C)	Winds (m s^{-1})
1800 5 Nov	1100 6 Nov	0.59	9.9	0.48	7.85	0.8	13.26	0.77	12.67	−4.37	NNE 1.4
1200 12 Nov	2000 12 Nov	0.29	2.3	0.2	1.7	0.36	2.85	0.4	3.3	−5.24	N 1.3
0900 17 Nov	1900 17 Nov	0.33	3.32	0.25	2.5	0.4	4.12	0.45	3.8	−9.59	NNE 0.94
0100 18 Nov	0300 18 Nov	0.17	0.28	0.11	0.19	0.18	0.3	0.18	0.29	−8.78	NNE 0.82
1700 20 Nov	1100 21 Nov	0.36	6.3	0.28	4.8	0.45	8.042	0.58	10.3	−6.99	ESE 2.13
1000 23 Nov	1500 23 Nov	0.5	2.57	0.46	2.28	0.74	3.7	0.73	3.64	−11.58	SE 3.8
1700 2 Dec	2000 2 Dec	0.56	1.67	0.46	1.35	0.75	2.24	X	X	−10.11	ESE 1.09
1600 7 Dec	0000 8 Dec	0.31	2.43	0.29	2.25	0.42	3.27	0.3	2.33	−17.08	SE 1.38
2200 12 Dec	0400 13 Dec	0.2	1.2	0.14	0.83	0.23	1.36	0.15	0.85	−7.9	N 2.66
2200 14 Dec	0100 15 Dec	0.19	0.76	0.16	0.63	0.24	0.95	0.21	0.81	−14.6	E 0.64
0500 23 Dec	0800 23 Dec	0.34	1.03	0.28	0.84	0.46	1.37	X	X	−9.63	ESE 2.07
0400 25 Dec	1000 25 Dec	0.52	3.13	0.52	3.12	0.78	4.7	0.55	3.34	−16.9	N 0.61
1100 29 Dec	1700 29 Dec	0.7	4.19	0.67	4.013	1.07	6.42	0.9	5.39	−15.16	NNE 1.38
0500 2 Jan	1200 3 Jan	0.19	4.79	0.15	3.52	0.23	5.75	0.17	3.88	−7.66	ESE 0.75
1800 5 Jan	0700 6 Jan	0.15	1.89	0.1	1.22	0.16	1.96	0.13	1.13	−10.43	N 3.53
2300 8 Jan	0300 9 Jan	0.83	2.74	0.77	2.23	1.23	3.76	0.7	1.83	−6.13	SE 0.97
1000 24 Jan	1900 24 Jan	0.5	4.45	0.56	5.04	0.8	7.22	0.32	2.84	−20.33	N 0.75
0100 25 Jan	0800 25 Jan	0.68	4.73	0.67	4.69	1.05	7.33	0.77	5.4	−15.03	N X
0000 10 Mar	0500 10 March	0.07	0.36	0.06	0.28	0.08	0.38	0.06	0.31	−14.35	SSW 0.3
1800 20 Mar	0000 21 March	0.29	1.71	0.2	1.15	0.33	1.9	0.29	1.6	−6.64	S 3.04
2100 21 Mar	0000 22 March	0.35	1.05	0.28	0.83	0.46	1.37	0.32	0.88	−6.88	S 0.56
0000 5 Apr	0200 5 Apr	0.363	0.73	0.25	0.48	0.42	0.81	0.13	0.25	X	X
1700 24 Apr	2100 24 Apr	0.34	1.37	0.24	0.94	0.4	1.6	0.17	0.64	−0.15	SE 1.39

TABLE A6. As in Table A1, but for intermittent snowfall events in Kiruna.

Start hour (UTC)	End hour (UTC)	Z_e–S (mm h^{-1})	Z_e–S (mm)	S19b6 (mm h^{-1})	S19b6 (mm)	S19b8 (mm h^{-1})	S19b8 (mm)	PIP (mm h^{-1})	PIP (mm)	Temp (°C)	Winds (m s^{-1})
1500 23 Nov	2100 24 Nov	0.67	19.6	0.59	17.2	0.97	28.4	0.6	17.83	−8.09	SE 2.33
0000 8 Dec	1300 10 Dec	0.45	20.1	0.4	16.7	0.61	27.8	0.33	15.7	−6.24	SE 2.6
2200 26 April	0800 27 April	0.29	2.03	0.3	1.3	0.36	2.13	0.05	2.14	0.72	SW 0.7

observe from space, and the Haukeliseter measurements will provide a better understanding of cloud-scale processes operating within orographic snow-bearing clouds and improve spaceborne snowfall retrievals. Also, it would be useful to continue to investigate differences between radar retrievals and surface observations.

Snowfall is inextricably linked to synoptic-scale processes and atmospheric circulation. This study illustrates the larger-scale circulation during the shallow, deep, and intermittent snowfall regimes. In a warming climate, changes in atmospheric circulation or in the frequency of intense snowfall events would imply changes to accumulation across the high latitudes. This work illustrates the utility of ground-based measurements in investigating snowfall processes. By continuing to study the regime-dependent processes and driving snowfall formation mechanisms using targeted observation systems, snowfall research continues to provide insight to the current state of snowfall and precipitation.

Acknowledgments. We thank the Norwegian Meteorological Institute for hosting instrumentation and sharing meteorological data at Haukeliseter, and specifically Mareile Wolff. We also thank the Swedish Institute for Space Physics for hosting instruments and sharing meteorological data at Kiruna, Sweden, and specifically Sandra Vázquez Martín and Thomas Kuhn. We thank Uwe Raffalski for information on the quality of wind measurements in Kiruna. Neither the European Commission nor ECMWF is responsible for any use that may be made of the Copernicus information or data it contains. The views, opinions, and findings contained in this paper are those of the authors and should not be construed as an official National Oceanic and Atmospheric Administration or U.S. government position, policy, or decision. This work was funded by NSF and NASA projects: 1531690, 1531930, 80NSSC18K0701, 80NSSC19K0712, 80NSSC18K0331, and 80NSSC20K0982.

Data availability statement. The MRR and PIP data are available locally at the University of Wisconsin–Madison and can be provided via FTP upon request.

APPENDIX

Snowfall Event Details

Tables A1–A6 include event details and instrument downtime for snowfall events in Haukeliseter and Kiruna. Event details include snowfall rates and accumulations and surface meteorological characteristics.

REFERENCES

Barthold, F. E., and D. A. Kristovich, 2011: Observations of the cross-lake cloud and snow evolution in a lake-effect snow event. *Mon. Wea. Rev.*, **139**, 2386–2398, https://doi.org/10.1175/MWR-D-10-05001.1.

Bennartz, R., F. Fell, C. Pettersen, M. D. Shupe, and D. Schuettemeyer, 2019: Spatial and temporal variability of snowfall over Greenland from CloudSat observations. *Atmos. Chem. Phys.*, **19**, 8101–8121, https://doi.org/10.5194/acp-19-8101-2019.

Bintanja, R., and F. Selten, 2014: Future increases in Arctic precipitation linked to local evaporation and sea-ice retreat. *Nature*, **509**, 479–482, https://doi.org/10.1038/nature13259.

——, and O. Andry, 2017: Towards a rain-dominated Arctic. *Nat. Climate Change*, **7**, 263–267, https://doi.org/10.1038/nclimate3240.

Collins, M., and Coauthors, 2013: Long-term climate change: Projections, commitments and irreversibility. *Climate Change 2013: The Physical Science Basis*, T. F. Stocker et al., Eds., Cambridge University Press, 1029–1136.

Cooper, S. J., N. B. Wood, and T. S. L'Ecuyer, 2017: A variational technique to estimate snowfall rate from coincident radar, snowflake, and fall-speed observations. *Atmos. Meas. Tech.*, **10**, 2557–2571, https://doi.org/10.5194/amt-10-2557-2017.

Copernicus Climate Change Service, 2017: ERA5: Fifth generation of ECMWF atmospheric reanalyses of the global climate. C3S Climate Data Store, accessed 18 March 2019, https://cds.climate.copernicus.eu.

Durán-Alarcón, C., B. Boudevillain, J. Grazioli, N. Souverijns, N. Van Lipzig, I. Gorodetskaya, and A. Berne, 2019: The vertical structure of precipitation at two stations in East Antarctica derived from Micro Rain Radars. *Cryosphere*, **13**, 247–264, https://doi.org/10.5194/tc-13-247-2019.

Eichenlaub, V. L., 1970: Lake effect snowfall to the lee of the great lakes: Its role in Michigan. *Bull. Amer. Meteor. Soc.*, **51**, 403–413, https://doi.org/10.1175/1520-0477(1970)051<0403:LESTTL>2.0.CO;2.

Eira, I. M. G., C. Jaedicke, O. H. Magga, N. G. Maynard, D. Vikhamar-Schuler, and S. D. Mathiesen, 2013: Traditional Sámi snow terminology and physical snow classification—Two ways of knowing. *Cold Reg. Sci. Technol.*, **85**, 117–130, https://doi.org/10.1016/j.coldregions.2012.09.004.

Elder, K., J. Dozier, and J. Michaelsen, 1991: Snow accumulation and distribution in an alpine watershed. *Water Resour. Res.*, **27**, 1541–1552, https://doi.org/10.1029/91WR00506.

Field, P. R., 2000: Bimodal ice spectra in frontal clouds. *Quart. J. Roy. Meteor. Soc.*, **126**, 379–392, https://doi.org/10.1002/qj.49712656302.

——, and A. Heymsfield, 2015: Importance of snow to global precipitation. *Geophys. Res. Lett.*, **42**, 9512–9520, https://doi.org/10.1002/2015GL065497.

Gorodetskaya, I. V., M. Tsukernik, K. Claes, M. F. Ralph, W. D. Neff, and N. P. Van Lipzig, 2014: The role of atmospheric rivers in anomalous snow accumulation in East Antarctica. *Geophys. Res. Lett.*, **41**, 6199–6206, https://doi.org/10.1002/2014GL060881.

Guan, B., and D. E. Waliser, 2015: Detection of atmospheric rivers: Evaluation and application of an algorithm for global studies. *J. Geophys. Res.*, **120**, 12 514–12 535, https://doi.org/10.1002/2015JD024257.

Hallett, J., 1965: Field and laboratory observations of ice crystal growth from the vapor. *J. Atmos. Sci.*, **22**, 64–69, https://doi.org/10.1175/1520-0469(1965)022<0064:FALOOI>2.0.CO;2.

Hoskins, B. J., and K. I. Hodges, 2002: New perspectives on the Northern Hemisphere winter storm tracks. *J. Atmos. Sci.*, **59**, 1041–1061, https://doi.org/10.1175/1520-0469(2002)059<1041:NPOTNH>2.0.CO;2.

Hou, A. Y., and Coauthors, 2014: The Global Precipitation Measurement Mission. *Bull. Amer. Meteor. Soc.*, **95**, 701–722, https://doi.org/10.1175/BAMS-D-13-00164.1.

Houze, R. A., Jr., and S. Medina, 2005: Turbulence as a mechanism for orographic precipitation enhancement. *J. Atmos. Sci.*, **62**, 3599–3623, https://doi.org/10.1175/JAS3555.1.

——, and Coauthors, 2017: The Olympic Mountains Experiment (OLYMPEX). *Bull. Amer. Meteor. Soc.*, **98**, 2167–2188, https://doi.org/10.1175/BAMS-D-16-0182.1.

Instanes, A., V. Kokorev, R. Janowicz, O. Bruland, K. Sand, and T. Prowse, 2016: Changes to freshwater systems affecting Arctic infrastructure and natural resources. *J. Geophys. Res. Biogeosci.*, **121**, 567–585, https://doi.org/10.1002/2015JG003125.

Jeoung, H., G. Liu, K. Kim, G. Lee, and E.-K. Seo, 2020: Microphysical properties of three types of snow clouds: Implication for satellite snowfall retrievals. *Atmos. Chem. Phys.*, **20**, 14 491–14 507, https://doi.org/10.5194/acp-20-14491-2020.

Kay, J. E., T. L'Ecuyer, A. Pendergrass, H. Chepfer, R. Guzman, and V. Yettella, 2018: Scale-aware and definition-aware evaluation of modeled near-surface precipitation frequency using CloudSat observations. *J. Geophys. Res.*, **123**, 4294–4309, https://doi.org/10.1002/2017JD028213.

Klugmann, D., K. Heinsohn, and H.-J. Kirtzel, 1996: A low cost 24 GHz FM-CW Doppler radar rain profiler. *Contrib. Atmos. Phys.*, **61**, 247–253.

Kneifel, S., and D. Moisseev, 2020: Long-term statistics of riming in nonconvective clouds derived from ground-based Doppler cloud radar observations. *J. Atmos. Sci.*, **77**, 3495–3508, https://doi.org/10.1175/JAS-D-20-0007.1.

——, M. Maahn, G. Peters, and C. Simmer, 2011: Observation of snowfall with a low-power FM-CW K-band radar (Micro Rain Radar). *Meteor. Atmos. Phys.*, **113**, 75–87, https://doi.org/10.1007/s00703-011-0142-z.

Knowles, N., M. D. Dettinger, and D. R. Cayan, 2006: Trends in snowfall versus rainfall in the western United States. *J. Climate*, **19**, 4545–4559, https://doi.org/10.1175/JCLI3850.1.

Kristovich, D. A., and Coauthors, 2017: The Ontario Winter Lake-Effect Systems field campaign: Scientific and educational adventures to further our knowledge and prediction of lake-effect storms. *Bull. Amer. Meteor. Soc.*, **98**, 315–332, https://doi.org/10.1175/BAMS-D-15-00034.1.

Kulie, M. S., and R. Bennartz, 2009: Utilizing spaceborne radars to retrieve dry snowfall. *J. Appl. Meteor. Climatol.*, **48**, 2564–2580, https://doi.org/10.1175/2009JAMC2193.1.

——, L. Milani, N. B. Wood, S. A. Tushaus, R. Bennartz, and T. S. L'Ecuyer, 2016: A shallow cumuliform snowfall census using spaceborne radar. *J. Hydrometeor.*, **17**, 1261–1279, https://doi.org/10.1175/JHM-D-15-0123.1.

Lavers, D. A., R. P. Allan, G. Villarini, B. Lloyd-Hughes, D. J. Brayshaw, and A. J. Wade, 2013: Future changes in atmospheric rivers and their implications for winter flooding in Britain. *Environ. Res. Lett.*, **8**, 034010, https://doi.org/10.1088/1748-9326/8/3/034010.

Lemonnier, F., and Coauthors, 2019: Evaluation of CloudSat snowfall rate profiles by a comparison with in situ micro-rain radar observations in East Antarctica. *Cryosphere*, **13**, 943–954, https://doi.org/10.5194/tc-13-943-2019.

Libbrecht, K. G., 2005: The physics of snow crystals. *Rep. Prog. Phys.*, **68**, 855–895, https://doi.org/10.1088/0034-4885/68/4/R03.

Liston, G., and M. Sturm, 2004: The role of winter sublimation in the Arctic moisture budget. *Hydrol. Res.*, **35**, 325–334, https://doi.org/10.2166/nh.2004.0024.

Liu, G., 2008: Deriving snow cloud characteristics from CloudSat observations. *J. Geophys. Res.*, **113**, D00A09, https://doi.org/10.1029/2007JD009766.

Liu, J., J. A. Curry, H. Wang, M. Song, and R. M. Horton, 2012: Impact of declining Arctic sea ice on winter snowfall. *Proc.*

Natl. Acad. Sci. USA, **109**, 4074–4079, https://doi.org/10.1073/pnas.1114910109.

Lund, M., C. Stiegler, J. Abermann, M. Citterio, B. U. Hansen, and D. van As, 2017: Spatiotemporal variability in surface energy balance across tundra, snow and ice in Greenland. *Ambio*, **46**, 81–93, https://doi.org/10.1007/s13280-016-0867-5.

Maahn, M., and P. Kollias, 2012: Improved Micro Rain Radar snow measurements using Doppler spectra post-processing. *Atmos. Meas. Tech.*, **5**, 2661–2673, https://doi.org/10.5194/amt-5-2661-2012.

——, C. Burgard, S. Crewell, I. V. Gorodetskaya, S. Kneifel, S. Lhermitte, K. Van Tricht, and N. P. van Lipzig, 2014: How does the spaceborne radar blind zone affect derived surface snowfall statistics in polar regions? *J. Geophys. Res.*, **119**, 13–604, https://doi.org/10.1002/2014JD022079.

Matrosov, S. Y., 2007: Modeling backscatter properties of snowfall at millimeter wavelengths. *J. Atmos. Sci.*, **64**, 1727–1736, https://doi.org/10.1175/JAS3904.1.

——, M. D. Shupe, and I. V. Djalalova, 2008: Snowfall retrievals using millimeter-wavelength cloud radars. *J. Appl. Meteor. Climatol.*, **47**, 769–777, https://doi.org/10.1175/2007JAMC1768.1.

McIlhattan, E. A., C. Pettersen, N. B. Wood, and T. S. L'Ecuyer, 2020: Satellite observations of snowfall regimes over the Greenland ice sheet. *Cryosphere*, **14**, 4379–4404, https://doi.org/10.5194/tc-14-4379-2020.

Morrison, H., G. De Boer, G. Feingold, J. Harrington, M. D. Shupe, and K. Sulia, 2012: Resilience of persistent Arctic mixed-phase clouds. *Nat. Geosci.*, **5**, 11–17, https://doi.org/10.1038/ngeo1332.

Mosimann, L., 1995: An improved method for determining the degree of snow crystal riming by vertical Doppler radar. *Atmos. Res.*, **37**, 305–323, https://doi.org/10.1016/0169-8095(94)00050-N.

Newman, A. J., P. A. Kucera, and L. F. Bliven, 2009: Presenting the Snowflake Video Imager (SVI). *J. Atmos. Oceanic Technol.*, **26**, 167–179, https://doi.org/10.1175/2008JTECHA1148.1.

Norin, L., A. Devasthale, T. L'Ecuyer, N. Wood, and M. Smalley, 2015: Intercomparison of snowfall estimates derived from the CloudSat Cloud Profiling Radar and the ground-based weather radar network over Sweden. *Atmos. Meas. Tech.*, **8**, 5009–5021, https://doi.org/10.5194/amt-8-5009-2015.

——, ——, and T. S. L'Ecuyer, 2017: The sensitivity of snowfall to weather states over Sweden. *Atmos. Meas. Tech.*, **10**, 3249–3263, https://doi.org/10.5194/amt-10-3249-2017.

Park, H., J. E. Walsh, Y. Kim, T. Nakai, and T. Ohata, 2013: The role of declining Arctic sea ice in recent decreasing terrestrial Arctic snow depths. *Polar Sci.*, **7**, 174–187, https://doi.org/10.1016/j.polar.2012.10.002.

Pettersen, C., R. Bennartz, A. J. Merrelli, M. D. Shupe, D. D. Turner, and V. P. Walden, 2018: Precipitation regimes over central Greenland inferred from 5 years of icecaps observations. *Atmos. Chem. Phys.*, **18**, 4715–4735, https://doi.org/10.5194/acp-18-4715-2018.

——, M. S. Kulie, L. F. Bliven, A. J. Merrelli, W. A. Petersen, T. J. Wagner, D. B. Wolff, and N. B. Wood, 2020a: A composite analysis of snowfall modes from four winter seasons in Marquette, Michigan. *J. Appl. Meteor. Climatol.*, **59**, 103–124, https://doi.org/10.1175/JAMC-D-19-0099.1.

——, and Coauthors, 2020b: The precipitation imaging package: Assessment of microphysical and bulk characteristics of snow. *Atmosphere*, **11**, 785, https://doi.org/10.3390/atmos11080785.

Putkonen, J., and G. Roe, 2003: Rain-on-snow events impact soil temperatures and affect ungulate survival. *Geophys. Res. Lett.*, **30**, 1188, https://doi.org/10.1029/2002GL016326.

Rasmussen, R., and Coauthors, 2012: How well are we measuring snow: The NOAA/FAA/NCAR winter precipitation test bed. *Bull. Amer. Meteor. Soc.*, **93**, 811–829, https://doi.org/10.1175/BAMS-D-11-00052.1.

Rawlins, M. A., C. Willmott, A. Shiklomanov, E. Linder, S. Frolking, R. B. Lammers, and C. Vörösmarty, 2006: Evaluation of trends in derived snowfall and rainfall across Eurasia and linkages with discharge to the Arctic Ocean. *Geophys. Res. Lett.*, **33**, L07403, https://doi.org/10.1029/2005GL025231.

——, and Coauthors, 2010: Analysis of the Arctic system for freshwater cycle intensification: Observations and expectations. *J. Climate*, **23**, 5715–5737, https://doi.org/10.1175/2010JCLI3421.1.

Riseth, J. Å., and Coauthors, 2011: Sámi traditional ecological knowledge as a guide to science: Snow, ice and reindeer pasture facing climate change. *Polar Rec.*, **47**, 202–217, https://doi.org/10.1017/S0032247410000434.

Rodgers, C., 2000: *Inverse Methods for Atmospheric Sounding*. World Scientific, 238 pp.

Roebber, P. J., S. L. Bruening, D. M. Schultz, and J. V. Cortinas Jr., 2003: Improving snowfall forecasting by diagnosing snow density. *Wea. Forecasting*, **18**, 264–287, https://doi.org/10.1175/1520-0434(2003)018<0264:ISFBDS>2.0.CO;2.

Rydzik, M., and A. R. Desai, 2014: Relationship between snow extent and midlatitude disturbance centers. *J. Climate*, **27**, 2971–2982, https://doi.org/10.1175/JCLI-D-12-00841.1.

Schirle, C. E., S. J. Cooper, M. A. Wolff, C. Pettersen, N. B. Wood, T. S. L'Ecuyer, T. Ilmo, and K. Nygård, 2019: Estimation of snowfall properties at a mountainous site in Norway using combined radar and in situ microphysical observations. *J. Appl. Meteor. Climatol.*, **58**, 1337–1352, https://doi.org/10.1175/JAMC-D-18-0281.1.

Schneider, U., A. Becker, P. Finger, A. Meyer-Christoffer, M. Ziese, and B. Rudolf, 2014: GPCC'S new land surface precipitation climatology based on quality-controlled in situ data and its role in quantifying the global water cycle. *Theor. Appl. Climatol.*, **115**, 15–40, https://doi.org/10.1007/s00704-013-0860-x.

Screen, J. A., and I. Simmonds, 2012: Declining summer snowfall in the Arctic: Causes, impacts and feedbacks. *Climate Dyn.*, **38**, 2243–2256, https://doi.org/10.1007/s00382-011-1105-2.

Serreze, M. C., and R. G. Barry, 2011: Processes and impacts of Arctic amplification: A research synthesis. *Global Planet. Change*, **77**, 85–96, https://doi.org/10.1016/j.gloplacha.2011.03.004.

Shupe, M. D., P. Kollias, P. O. G. Persson, and G. M. McFarquhar, 2008: Vertical motions in Arctic mixed-phase stratiform clouds. *J. Atmos. Sci.*, **65**, 1304–1322, https://doi.org/10.1175/2007JAS2479.1.

Skofronick-Jackson, G. M., B. T. Johnson, and S. J. Munchak, 2013: Detection thresholds of falling snow from satellite-borne active and passive sensors. *IEEE Trans. Geosci. Remote Sens.*, **51**, 4177–4189, https://doi.org/10.1109/TGRS.2012.2227763.

——, and Coauthors, 2015: Global Precipitation Measurement Cold Season Precipitation Experiment (GCPEX): For measurement's sake, let it snow. *Bull. Amer. Meteor. Soc.*, **96**, 1719–1741, https://doi.org/10.1175/BAMS-D-13-00262.1.

Smalley, M., T. L'Ecuyer, M. Lebsock, and J. Haynes, 2014: A comparison of precipitation occurrence from the NCEP Stage IV QPE product and the *CloudSat* Cloud Profiling Radar. *J. Hydrometeor.*, **15**, 444–458, https://doi.org/10.1175/JHM-D-13-048.1.

Sodemann, H., and A. Stohl, 2013: Moisture origin and meridional transport in atmospheric rivers and their association with

multiple cyclones. *Mon. Wea. Rev.*, **141**, 2850–2868, https://doi.org/10.1175/MWR-D-12-00256.1.

Sokolov, A. A., N. A. Sokolova, R. A. Ims, L. Brucker, and D. Ehrich, 2016: Emergent rainy winter warm spells may promote boreal predator expansion into the Arctic. *Arctic*, **69**, 121–129, https://doi.org/10.14430/arctic4559.

Souverijns, N., A. Gossart, S. Lhermitte, I. Gorodetskaya, S. Kneifel, M. Maahn, F. L. Bliven, and N. Van Lipzig, 2017: Estimating radar reflectivity-snowfall rate relationships and their uncertainties over Antarctica by combining disdrometer and radar observations. *Atmos. Res.*, **196**, 211–223, https://doi.org/10.1016/j.atmosres.2017.06.001.

Speirs, P., M. Gabella, and A. Berne, 2017: A comparison between the GPM Dual-Frequency Precipitation Radar and ground-based radar precipitation rate estimates in the Swiss Alps and plateau. *J. Hydrometeor.*, **18**, 1247–1269, https://doi.org/10.1175/JHM-D-16-0085.1.

Stark, D., B. A. Colle, and S. E. Yuter, 2013: Observed microphysical evolution for two East Coast winter storms and the associated snow bands. *Mon. Wea. Rev.*, **141**, 2037–2057, https://doi.org/10.1175/MWR-D-12-00276.1.

Stephens, G. L., and Coauthors, 2002: The *CloudSat* mission and the A-Train: A new dimension of space-based observations of clouds and precipitation. *Bull. Amer. Meteor. Soc.*, **83**, 1771–1790, https://doi.org/10.1175/BAMS-83-12-1771.

Tamang, S. K., A. M. Ebtehaj, A. F. Prein, and A. J. Heymsfield, 2020: Linking global changes of snowfall and wet-bulb temperature. *J. Climate*, **33**, 39–59, https://doi.org/10.1175/JCLI-D-19-0254.1.

Tiira, J., D. N. Moisseev, A. von Lerber, D. Ori, A. Tokay, L. F. Bliven, and W. Petersen, 2016: Ensemble mean density and its connection to other microphysical properties of falling snow as observed in southern Finland. *Atmos. Meas. Tech.*, **9**, 4825–4841, https://doi.org/10.5194/amt-9-4825-2016.

Vavrus, S., 2007: The role of terrestrial snow cover in the climate system. *Climate Dyn.*, **29**, 73–88, https://doi.org/10.1007/s00382-007-0226-0.

Verlinde, J., and Coauthors, 2007: The Mixed-Phase Arctic Cloud Experiment. *Bull. Amer. Meteor. Soc.*, **88**, 205–222, https://doi.org/10.1175/BAMS-88-2-205.

von Lerber, A., D. Moisseev, L. F. Bliven, W. Petersen, A.-M. Harri, and V. Chandrasekar, 2017: Microphysical properties of snow and their link to Z_e–S relations during BAECC 2014. *J. Appl. Meteor. Climatol.*, **56**, 1561–1582, https://doi.org/10.1175/JAMC-D-16-0379.1.

——, ——, D. A. Marks, W. Petersen, A.-M. Harri, and V. Chandrasekar, 2018: Validation of GMI snowfall observations by using a combination of weather radar and surface measurements. *J. Appl. Meteor. Climatol.*, **57**, 797–820, https://doi.org/10.1175/JAMC-D-17-0176.1.

Wang, Y., B. Geerts, and Y. Chen, 2016: Vertical structure of boundary layer convection during cold-air outbreaks at Barrow, Alaska. *J. Geophys. Res.*, **121**, 399–412, https://doi.org/10.1002/2015JD023506.

Ware, E. C., D. M. Schultz, H. E. Brooks, P. J. Roebber, and S. L. Bruening, 2006: Improving snowfall forecasting by accounting for the climatological variability of snow density. *Wea. Forecasting*, **21**, 94–103, https://doi.org/10.1175/WAF903.1.

Wolff, M., K. Isaksen, A. Petersen-Øverleir, K. Ødemark, T. Reitan, and R. Brækkan, 2015: Derivation of a new continuous adjustment function for correcting wind-induced loss of solid precipitation: Results of a Norwegian field study. *Hydrol. Earth Syst. Sci.*, **19**, 951–967, https://doi.org/10.5194/hess-19-951-2015.

Wood, N. B., T. S. L'Ecuyer, A. J. Heymsfield, and G. L. Stephens, 2015: Microphysical constraints on millimeter-wavelength scattering properties of snow particles. *J. Appl. Meteor. Climatol.*, **54**, 909–931, https://doi.org/10.1175/JAMC-D-14-0137.1.